Ocean Engineering 357 (2026) 125327

Contents lists available at ScienceDirect

Ocean Engineering

journal homepage: www.elsevier.com/locate/oceaneng

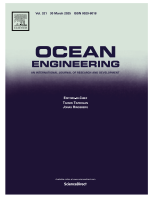

Research paper

Assessing ice risks for offshore wind development in the Great Lakes

M. Javad Javaherian [a,b,*], Hazem Abdelhady [c], David Cannon [b,*], Jia Wang [d], Ayumi Fujisaki-Manome [b,e], Lei Zuo [a,*]

[a] Department of Naval Architecture and Marine Engineering, University of Michigan, Ann Arbor, 48109, Michigan, USA
[b] Cooperative Institute for Great Lakes Research, University of Michigan, Ann Arbor, 48109, Michigan, USA
[c] Department of Geography, Texas A&M University, College Station, 77843, Texas, USA
[d] NOAA Great Lakes Environmental Research Laboratory, Ann Arbor, 48108, Michigan, USA
[e] Department of Climate and Space Sciences and Engineering, University of Michigan, Ann Arbor, 48109, Michigan, USA

ARTICLE INFO

Keywords:
Offshore wind
Great lakes
Ice load
Ice risk
Icing
Hindcast

ABSTRACT

The Laurentian Great Lakes represent a vast and largely untapped potential for offshore wind energy that is crucial for regional decarbonization, energy security, and economic development. However, seasonal freshwater ice introduces unique engineering and operational risks, especially since limited availability of ice data poses challenges to safe and cost-effective design. To address this gap, we apply a fully coupled three-dimensional hydrodynamic-ice model (FVCOM–CICE) to simulate ice conditions across all five Great Lakes over an 83-year period (1940–2022). The model, validated against satellite and in-situ measurements, yields detailed spatial and temporal distributions of ice concentration, thickness, and velocity. To provide an integrated assessment for wind energy development, a composite ice intensity index is introduced by synthesizing ice momentum, packed ice risk, and icing severity. This index enables site-specific quantification of overall ice hazards to support more robust wind turbine siting, design, and risk mitigation. A case study is also presented to demonstrate practical applications of simulated ice data in evaluating ISO/IEC design ice load limits on offshore wind platforms. Results reveal that extreme ice hazards are prevalent in Lake Erie, Lake Huron, and parts of Lake Superior, while Lake Ontario and central and southern regions of Lake Michigan exhibit consistently lower ice risks. This paper offers a foundation for resilient offshore wind infrastructure and supports multi-criteria decision frameworks in this region.

1. Introduction

The Laurentian Great Lakes represent a region of substantial wind energy potential, with overall estimated capacities exceeding 743 GW (Musial and Ram, 2010), of which 575 GW are located within U.S. waters (Lopez et al., 2022). Leveraging this resource is vital to enable the eight surrounding U.S. states to meet ambitious decarbonization goals set for 2040–2050 (Sutherland and Scanlan, 2025), while also advancing renewable energy adoption, enhancing energy security, and stimulating local economies. Despite this promise, the unique environment of the Great Lakes presents substantial technical barriers to offshore wind development. The recurring formation of seasonal freshwater ice introduces significant structural and operational complexities for both fixed-bottom and floating offshore wind turbines in this region (Musial and Ram, 2010; Musial et al., 2023; Javaherian et al., 2025b).

Some of the ice hazards associated with offshore wind structures in cold-climate regions are illustrated in Fig. 1. For fixed offshore wind platforms, the ice-structure interaction can induce substantial static and dynamic loads that compromise long-term structural integrity and accelerate fatigue (Hammer et al., 2023; Zou et al., 2024; Huang et al., 2025). Moreover, specific ice conditions can trigger the non-linear phenomenon of Ice-Induced Vibration (IIV), which can lead to Frequency Lock-In (FLI) phenomenon, resulting in excessive structural vibration and fatigue damage (Zhu et al., 2021; Wu et al., 2024b). Floating offshore wind platforms in cold-climate regions are also highly susceptible to ice accumulation and severe impacts by moving ice floes that can impair the platform stability, impose critical damage to mooring systems, and compromise energy production (Barooni et al., 2022; NYSERDA, 2022). Underestimating ice loads can cause structural failure and/or major incidents for maritime structures (Wu et al., 2024a; Fang et al., 2000). On the other hand, overestimating ice loads due to high uncertainty may result in overly conservative structural designs, leading to increased construction and installation costs (Musial et al., 2023).

* Corresponding authors.
E-mail addresses: mjava@umich.edu (M.J. Javaherian), djcannon@umich.edu (D. Cannon), leizuo@umich.edu (L. Zuo).

https://doi.org/10.1016/j.oceaneng.2026.125327
Received 18 December 2025; Received in revised form 24 March 2026; Accepted 26 March 2026
Available online 14 April 2026

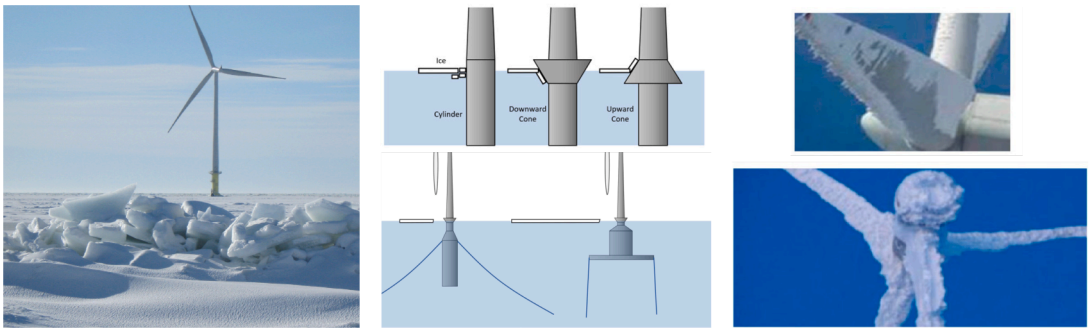

Fig. 1. Ice hazards associated with offshore wind platforms in cold-climate regions. Plots show a) packed ice around a turbine [credit: from N.N. for Suomen Hyötytuuli (NREL, 2023)], b) ice impacting fixed (top) and floating (bottom) offshore wind turbines [credit: NYSERDA (2022)], and c) icing on the turbine blades [credit: Okulov et al. (2021)].

As an additional consideration, air-sea interactions near offshore wind turbines can result in water droplets being sprayed onto both the platform and turbine blades. In the cold climate of the Great Lakes, these droplets can freeze rapidly and lead to the accumulation of ice on structural components (Fig. 1(c)). Ice buildup imposes additional, often asymmetric, loading on the platform and turbine, which can compromise structural stability and integrity. Furthermore, icing on turbine blades alters their shape and surface roughness, significantly deteriorating the aerodynamic performance of the turbine. Icing can also contribute to ice-throwing risks that can pose serious safety hazards to nearby structures or personnel. Studies indicate that icing is a major source of generation loss in cold-climate regions that can result in power losses ranging from 20–50% (Zhang et al., 2024; Etemaddar et al., 2014; Tammelin et al., 2000).

Unlike ocean waters, the freshwater in the Great Lakes freezes at a higher temperature due to its lower salinity. The absence of salinity also results in harder, denser, and more persistent ice formation. This makes both ice loads and icing events in the Great Lakes particularly severe and potentially more damaging than those in other marine environments. Therefore, offshore wind turbines in this region must be strategically sited, robustly engineered, and diligently maintained to withstand these unique ice-related challenges. Consequently, gaining a thorough understanding of ice properties, their seasonal variability, and the occurrence of extreme ice events is crucial. Such understanding ensures that offshore wind sites and structures in the Great Lakes are designed and operated with reliability, economic efficiency, and resilience to a changing climate.

Despite the eminence of ice hazards, observational data on ice conditions in the Great Lakes remain significantly limited in both extent and accuracy, which poses major challenges for offshore wind development. Satellite-driven ice observations, such as those provided by the U.S. National Ice Center (NIC), offer valuable data on ice concentration but are constrained by factors like cloud cover interference and temporal and spatial averaging, which can obscure the local variations critical for engineering assessments. Additionally, other essential ice parameters, such as ice thickness and velocity, are either sparsely available or not captured in these observational records. While in-situ measurements offer greater detail, they are scarce, geographically isolated, and insufficient to yield comprehensive lake-wide insights. These gaps in data availability and quality hinder the ability to accurately characterize ice loads and dynamics essential for structural design and operational planning. Importantly, recent assessments, including the Musial et al. (2023) report, highlight that the characterization of ice conditions and extreme ice load values remains poorly represented and is a major missing component in Great Lakes offshore wind research. This underlines a critical need for improved ice modeling to inform safe and cost-effective infrastructure development.

To address this gap, this study uses a three-dimensional hydrodynamic-ice modeling framework to simulate historical ice conditions in the Great Lakes from 1940 to 2022. The modeling approach, utilizing FVCOM–CICE, captures detailed lake-wide ice behavior in terms of concentration, thickness, and velocity. By generating an extensive 83-year record of ice data, this work provides a detailed analysis of long-term spatial and temporal ice patterns relevant to offshore wind energy development. The simulations are rigorously validated against satellite observations and in-situ measurements, demonstrating strong model skill. Key outputs include spatial maps of mean, extreme maximum, and 90th percentile ice metrics to identify areas with relatively low ice hazards for informed project siting and design. Additionally, this research introduces a novel composite ice hazard index that integrates ice momentum, packed ice pressure, and icing severity. This index provides a comprehensive assessment of ice risks, capturing both the mechanical and environmental challenges unique to the Great Lakes. By offering actionable insights into these hazards, the study supports more informed offshore wind siting and design decisions. Ultimately, this work advances the characterization of ice-related risks, helping to address one of the most significant technical barriers to the development of future offshore wind infrastructure in the Great Lakes region.

The remainder of this paper is structured as follows: Section 2 details the datasets employed and elaborates on the numerical configuration of the coupled FVCOM–CICE hydrodynamic-ice model used to simulate Great Lakes ice conditions over the historical period 1940–2022. Section 3 presents the validation of the model outputs against satellite and in-situ observations, followed by a comprehensive analysis of the spatial and temporal patterns of ice concentration, thickness, and velocity across the lakes. Section 4 introduces derived metrics such as ice momentum, packed ice probability, and icing severity, culminating in an integrated ice intensity index for hazard assessment. Additionally, a case study is presented in this section that demonstrates how the long-term hindcast data can inform site-specific load analysis based on common design standards for offshore platforms. Finally, Section 5 summarizes the key findings and discusses their implications for offshore wind siting and design in the Great Lakes.

2. Methodology and data

2.1. Data

Several datasets were utilized in this study to support both the setup and validation of the coupled FVCOM–CICE hydrodynamic–ice model simulations. Ice simulations were primarily forced using the ERA5 atmospheric reanalysis product (Hersbach et al., 2020), a fifth-generation dataset produced by the European Centre for Medium-Range Weather

Forecasts (ECMWF). ERA5 offers hourly meteorological fields (e.g., wind speed, surface air temperature, pressure, precipitation, and radiation fluxes) at approximately 31 km spatial resolution from 1940 to the present. These data provide thorough and temporally consistent coverage for all five Great Lakes, making ERA5 an ideal baseline dataset for long-term hindcast studies.

Model sensitivity analyses revealed that ERA5 exhibits a persistent cold bias in winter air temperature over Lake Superior (see discussions for Fig. 4(a) and (b)), a deficiency also documented in recent reanalysis studies and hydrodynamic modeling work across the region (Minallah and Steiner, 2021; Simmons et al., 2021; Wang et al., 2025). This discrepancy is mainly attributed to poorly parameterized lake-atmosphere interactions in the ERA5 reanalysis product, posing a significant bias for Lake Superior, as it has the largest depth and surface area among the Great Lakes (Simmons et al., 2021). Consequently, this leads to high-biased ice cover and ice thickness simulations during the core winter months. To address this issue, Lake Superior simulations were re-run using meteorological forcing from the North American Regional Reanalysis (NARR) (Mesinger et al., 2006). NARR provides 3-hourly meteorological variables at a nominal 32 km resolution with improved representation of regional climate dynamics over North America. Replacing ERA5 with NARR for Lake Superior substantially improved the predicted ice data, aligning the results more closely with the satellite observations. The other four lakes retained the ERA5 dataset as atmospheric forcing, as no significant systematic biases were observed in those basins. This enabled a longer hindcast for these lakes covering years of 1940-2022 using ERA5 forcing, while NARR data are only available for 1979 onward.

Bathymetry data for the model grid were obtained from the NOAA National Centers for Environmental Information (NCEI) and the National Geophysical Data Center (NGDC) joint database. For model validation, remote-sensing datasets from the NOAA Great Lakes Environmental Research Laboratory (GLERL) were utilized, including satellite-derived ice concentration and thickness data processed by the U.S. National Ice Center (NIC). These products were employed to assess both the temporal and spatial variability of modeled ice cover from 1973 onward. In addition, in-situ ice thickness measurements collected using an ASL Environmental Sciences Shallow Water Ice Profiler (SWIP) in Lake Erie during the winter of 2011 (Hawley et al., 2018) provided independent validation for simulated ice thickness data. Acoustic Doppler Current Profiler (ADCP) measurements from Lake Superior (Titze and Austin, 2016) were also used to validate modeled ice velocities.

2.2. Hydrodynamic-ice modeling framework

The numerical setup for this study employs the FVCOM–CICE framework as a sophisticated, fully coupled, and three-dimensional hydrodynamic-ice modeling system that is specifically configured for the Great Lakes region.

The core framework utilizes the Finite Volume Community Ocean Model (FVCOM), which is a widely employed unstructured-grid and finite-volume ocean model (Chen et al., 2003, 2006). This model features an unstructured mesh of triangular control elements in the horizontal domain and employs terrain-following σ-coordinates in the vertical domain. FVCOM is designed to compute fluxes through solving the governing primitive equations and provide high-resolution simulations of fluid motion, temperature, and other dynamic properties.

Ice dynamics are incorporated by coupling FVCOM with the unstructured grid version of the CICE model, which is developed by Gao et al. (2011) as an advanced adaptation of the original Los Alamos Community Ice Code (CICE). This model employs a sophisticated unstructured-grid and finite-volume approach and uses energy-conserving thermodynamics (Hunke and Lipscomb, 2006), energy-driven ridging schemes (Thorndike et al., 1975; Hibler III, 1979; Lipscomb et al., 2007), and elastic-viscous-plastic momentum equations (Hunke and Dukowicz, 1997; Hunke, 2001; Hunke and Dukowicz, 2002) to effectively simulate key ice properties, including ice concentration, velocity, and thickness. Coupled with CICE, the specific FVCOM version utilized in this study (ver. 4.4.2) has been successfully tested and validated for the Great Lakes (Abdelhady et al., 2025a,b).

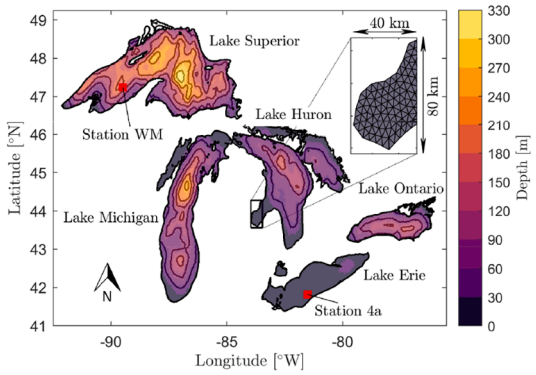

Fig. 2. The Great Lakes and their bathymetry forming the computational domain of this study. The south-western region of Lake Huron, also known as Saginaw Bay, is magnified with detailed view to depict the unstructured grid utilized in the FVCOM–CICE framework.

In this study, the above-mentioned FVCOM–CICE model is employed to simulate ice behavior in Lakes Michigan, Huron, Erie, and Ontario during the 1940-2022 period. The simulations in Lake Superior are restricted to 1979-2022 due to limited NARR forcing data availability.

Fig. 2 illustrates the computational domain, encompassing Lakes Superior, Michigan, Huron, Erie, and Ontario. The domain utilizes an unstructured triangular grid with an average horizontal resolution of approximately 3.5 km (see the detailed view of the southwestern part of Lake Huron, Saginaw Bay). It is important to note that the model neglects connecting channels and river inflows, treating the basins as largely isolated except for the natural connection between Lakes Michigan and Huron. Vertically, the model is resolved by 21 terrain-following σ-levels, which are strategically designed to enhance resolution near the surface and bottom boundaries for accurate boundary layer process capture. The model is initialized on January 1st, 1940 (1979 in the case of Lake Superior), with a uniform temperature of 4°C across all lakes. This temperature serves solely as a reasonable starting point for early-winter conditions in the Great Lakes and has negligible effects on the long-term results, as the model equilibrates over the initial spin-up period. The simulations were configured with a 3-second external time step and a 60-second internal time step, using a split ratio of 20. Throughout the simulation period, 3-hourly output is recorded for subsequent analysis. Further technical details of the model setup and configurations can be found in Cannon et al. (2024), and Abdelhady et al. (2025b). Furthermore, for a systematic analysis on the sensitivity of other model parameters readers are referred to Cannon et al. (2024) and Javaherian et al. (2025a).

3. Simulation results

3.1. Validation

To initiate model validation, the lake-averaged ice cover was evaluated for each lake. This metric, denoted as IC, quantifies the mean ice concentration over the lake's surface. The ice cover is computed as the ratio of the sum of the products of ice concentration and the area of each computational cell within the lake to the total lake area, as defined by:

$$IC = \frac{\sum_{n=1}^{N} \left[A_n \, a_{ice,n} \right]}{\sum_{n=1}^{N} A_n}, \tag{1}$$

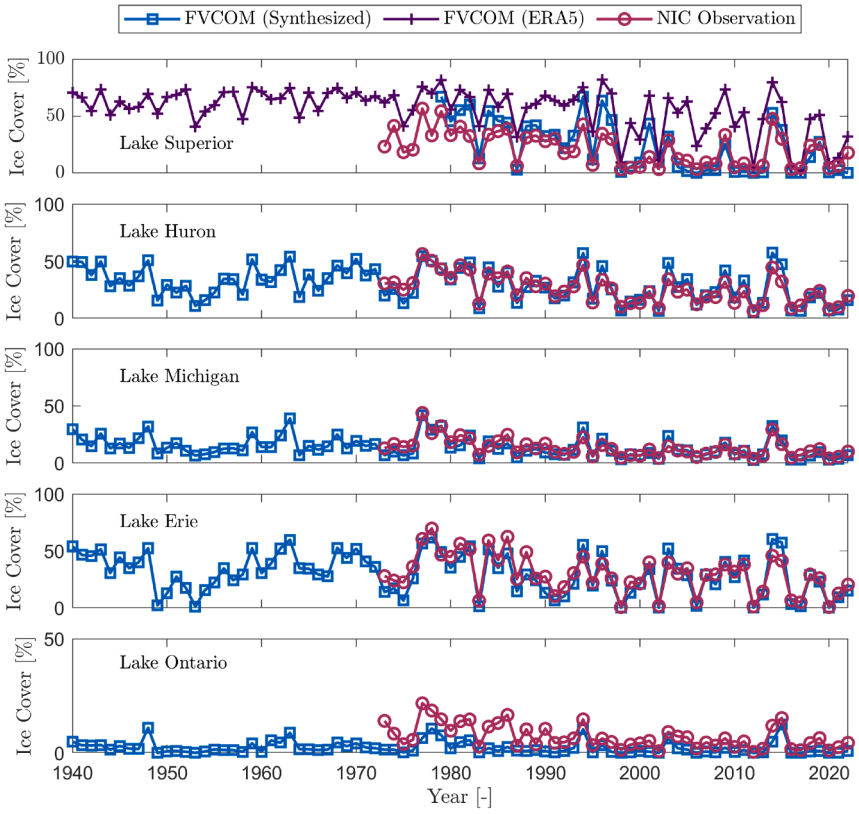

Fig. 3. Lake-averaged ice cover in Lakes Superior, Huron, Michigan, Erie, and Ontario in different years. The FVCOM (ERA5) model denotes the simulation for Lake Superior only that is driven by ERA5 forcing dataset. The FVCOM (Synthesized) model refers to simulations driven by the ERA5 dataset for Lakes Huron, Michigan, Erie, and Ontario, whereas Lake Superior's simulation uses the NARR forcing dataset. The rest of the paper is based on the FVCOM (Synthesized) model.

where A_n represents the area of the n^{th} cell in the lake domain, $a_{ice,n}$ is the ice concentration in that cell, and N is the total number of cells covering the lake.

Fig. 3 presents a comparison between the simulated lake-averaged ice cover and satellite-derived observations from the National Ice Center (NIC), which have been available since 1973 and serve as the validation benchmark for this study. The FVCOM (Synthesized) terminology used here refers to simulations driven by the ERA5 dataset for Lakes Huron, Michigan, Erie, and Ontario, whereas NARR dataset for Lake Superior. Overall, the model closely replicates the observed ice cover across all lakes, capturing both low and high ice years during the extended study period. Notably, the simulated ice cover for Lake Superior shows a marked improvement when using NARR forcing compared to the ERA5-based estimates, labeled as FVCOM (ERA5). The overestimation of ice cover in the ERA5-driven Lake Superior simulation is attributed to a cold bias in the ERA5 winter air temperature forcing (see Fig. 4(a) and (b)). The results and analyses presented in this paper are based exclusively on the FVCOM synthesized model that incorporates these improvements.

The cold bias present in ERA5 air temperature data over Lake Superior is illustrated in Fig. 4(a), for two representative winter seasons: 1983 and 2011. In this figure, air temperature from ERA5 and NARR is compared against daily averaged measurements from multiple coastal weather stations around the lake (Fujisaki-Manome et al., 2024). It is evident that ERA5 consistently reports significantly lower temperatures than both NARR and the station-based observations (reaching up to 10° C difference). To evaluate this for a longer period, Fig. 4(b) illustrates the differences between lake-averaged ERA5 and NARR air temperature over Lake Superior during their common period (1979-2022). This difference is quantified through boxplots summarizing the monthly distribution of temperature differences, with median values showing ERA5 temperatures to be consistently lower during winter months. Since air temperature serves as a key forcing input in the modeling framework, this cold bias can lead to substantial overestimation of ice cover in simulations. As shown in Fig. 4(a), NARR provides a closer approximation to observed temperatures, thus improving model accuracy for Lake Superior. The forcing correction, using NARR data to force simulations for Lake Superior, is essential for reliable modeling outcomes as demonstrated by the improved agreement between simulations using NARR forcing and observed ice data for this lake (Fig. 3). Despite this limitation, the ice cover simulations for the other Great Lakes show good agreement with observed data (Fig. 3). It is also worth emphasizing that ERA5 was selected for this work due to its longer historical record, spanning from 1940 to the present, compared with NARR's coverage beginning in 1979.

Fig. 5 presents a detailed comparison between NIC observed ice concentrations (Fig. 5(a)–(c)) and the FVCOM model simulations (Fig. 5(d)–(f)) for January, February, and March of 2011. The model demonstrates strong consistency with the observed data, effectively reproducing the seasonal evolution of ice formation and melting throughout the entire domain. In particular, the simulation captures the progressive increase in ice coverage during January and the subsequent decline during March. It is worthwhile to mention that some lower-latitude regions, such as Lake Erie, exhibit higher ice concentrations compared to higher-latitude lakes. This is mainly due to shallow bathymetry (see Fig. 2) and lower heat storage in these regions, which enable faster cooling and freeze-up compared to deeper northern lakes. As noted earlier, the model does not incorporate streamflow forcing from river inflows, which could also affect regional ice dynamics and may contribute to discrepancies between simulations and observations in the vicinity of the channels and rivers. However, neglecting connecting channels and river inflows is a standard simplification in lake-wide Great Lakes

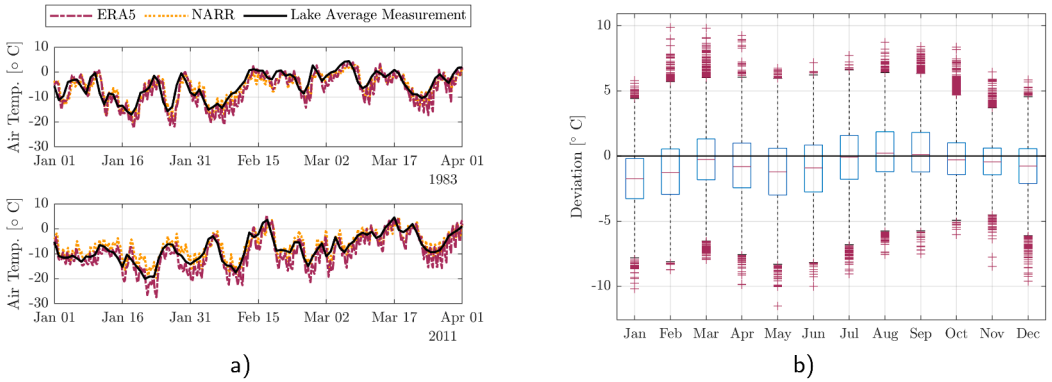

Fig. 4. The ERA5 cold-biased air temperature at Lake Superior; a) Comparison of lake-averaged air temperature between ERA5 and NARR datasets for the representative winter seasons of 1983 and 2011. The lake-averaged measurements correspond to daily averages recorded at multiple weather stations encircling Lake Superior (Fujisaki-Manome et al., 2024). b) Boxplot showing the deviation between lake-averaged air temperature from ERA5 and NARR datasets (ERA5–NARR) for the common period (1979–2022). The lower and upper box boundaries indicate the 25th and 75th percentiles, respectively. The central line denotes the median, whiskers extend to 1.5 × the interquartile range, and outliers are plotted as individual points.

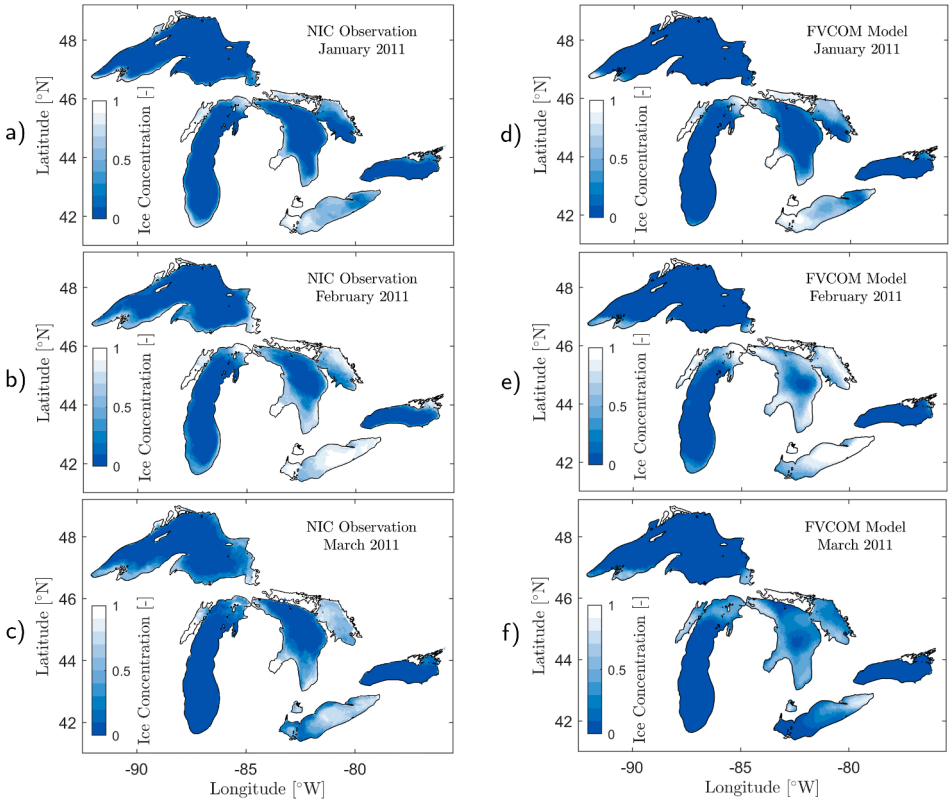

Fig. 5. Comparison between monthly average ice concentration from the proposed FVCOM framework with NIC observations in winter 2011. The NIC satellite data (a, b, and c) are plotted with FVCOM predictions (d, e, and f) for months of January (a and d), February (b and e), and March (c and f) 2011.

hydrodynamic-ice models, justified by their minor contribution to total lake volume and basin-averaged ice properties (Fujisaki et al., 2013).

To assess the temporal accuracy of the model, ice cover predictions at Station 4a (see Fig. 2) during February 2011 were compared against observational datasets. Fig. 6(a) illustrates the time series of ice concentration from the FVCOM model alongside NIC satellite-driven observations. Both datasets display consistently high ice cover, often exceeding 90%, during the first half of February, followed by a sharp decline around February 17 to values close to 0%, and a subsequent rebound towards the end of the month. The model successfully captures the timing and magnitude of these fluctuations, though it exhibits slightly more variability than the observations. It is important to acknowledge that uncertainties inherent in the NIC data, such as cloud cover interference, may contribute to some discrepancies, as shown in Fig. 13(f) of Javaherian et al. (2025a). Fig. 6(b) presents a comparison of ice thickness between the FVCOM simulations, NIC estimates, and in-situ measurements from Hawley et al. (2018). The modeled ice thickness aligns well with measured data and accurately reflects both the temporal trends and magnitude throughout the period. While the ice thickness remains close to 0.5 m at the first half of February, a reduction in the ice thickness is observed starting from February 15. This matches with the reduction in the ice concentration at this time, as was observed in Fig. 6(a). The ice thickness slightly increases towards the end of February, as higher ice concentration values were observed in this period.

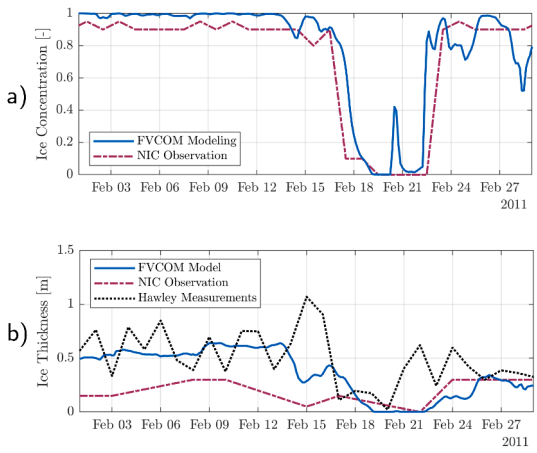

Fig. 6. FVCOM predictions are evaluated against observations and measurements at Station 4a in Lake Erie (see Fig. 2). The comparisons include model predictions with: a) NIC ice concentration data, and b) NIC-driven estimates of ice thickness alongside direct in-situ measurements reported by Hawley et al. (2018).

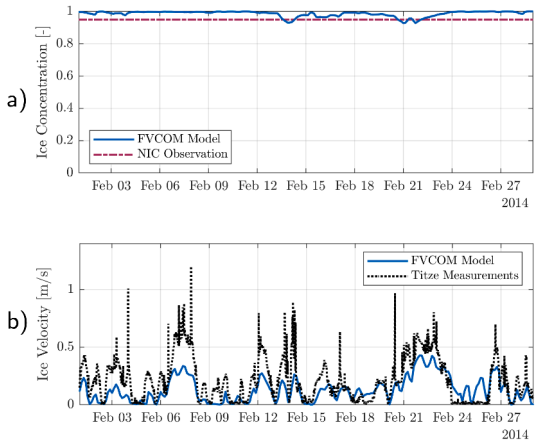

Fig. 7. FVCOM results are compared with observations and measurements at Station WM in Lake Superior (see Fig. 2). Results show comparisons between simulations and a) NIC ice concentration data, b) Titze and Austin (2016) ice velocity measurements.

Fig. 7 demonstrates ice concentration (Fig. 7(a)) and ice velocity (Fig. 7(b)) at Station WM, located in Lake Superior (see Fig. 2), during February 2014. This location and time frame were chosen to enable comparison between FVCOM-predicted ice velocities and measurements reported by Titze and Austin (2016). With ice concentration remaining in the range of 95–100%, the ice velocity exhibits significant fluctuations throughout the month, driven primarily by varying wind speeds at this station. Fig. 7(b) reveals that the predicted ice velocity, which is an important factor in the FLI evaluation, is slightly underestimated compared to the measurements. This is primarily attributed to the coarse spatial resolution of the domain (~3.5 km) and ERA5/NARR atmospheric forcing (~31-32 km) compared to the localized point measurements at Station WM. Forcing fields can be downscaled or corrected using high-resolution meteorological observations at target sites to yield more accurate ice velocity predictions and consequently, refined site-specific FLI analysis. Yet, the comparison shows reasonable accuracy in predicted ice concentration and velocity results that reinforces the model's capability to reliably reproduce key ice properties in the Great Lakes.

3.2. Ice concentration

Ice concentration, the fraction of surface area covered with ice, is a critical factor for the design and operation of offshore wind structures. This parameter reflects the frequency and extent of ice exposure to the platform that directly impacts operational safety, maintenance planning, and material selection for the structure. Fig. 8 provides a detailed analysis of ice concentration variability across the Great Lakes to highlight regional differences that inform site selection and structural considerations.

Fig. 8(a) displays the spatial patterns of mean annual maximum ice concentration for the Great Lakes over the study period. This metric is computed by first identifying the maximum ice concentration at each location for each year, then calculating the average of these maxima across all years. The results indicate that Lakes Erie and Lake Huron consistently exhibit the highest maximum average ice concentrations, with peak values often exceeding 90%. Coastal zones, such as northern Lake Michigan, also illustrate higher average ice concentrations as they generally tend to freeze more quickly due to their shallow depth and associated low thermal inertia. Conversely, Lake Ontario predominantly experiences ice concentration below 30%, as central and southern regions of Lake Michigan generally remain under 40%.

Fig. 8(b) maps the maximum annual ice concentration or, in other words, the most extreme maximum ice concentration recorded over the full study period at each grid cell. The map reveals that the entire surface area of the Great Lakes has experienced full ice coverage at least once over the recorded period. This emphasizes the potential spatial extent of ice during the most severe winter conditions.

Lastly, Fig. 8(c) shows the 90th percentile ice concentration in winters for the Great Lakes. This metric reflects the ice cover values that are exceeded only 10% of the time, reflecting frequently high but not extreme ice conditions. This figure reveals persistent high ice concentrations, often above 90%, in Lake Superior, Lake Erie, Lake Huron, and northern Lake Michigan, where coastal areas frequently see high ice concentration values. In contrast, Lake Ontario and the central and southern basin of Lakes Michigan generally experience considerably lower ice concentrations that are frequently below 10%.

3.3. Ice thickness

Ice thickness is another key parameter influencing offshore infrastructure design, as it dictates the vertical extent to which structures must resist ice forces and determines the magnitude of ice-induced loads. Accurately characterizing ice thickness variability is therefore vital for engineering design in ice-prone environments. An analysis of ice thickness variability over the Great Lakes is presented in Fig. 9. In this figure, only days with ice concentration exceeding 5% are taken into account, and thus, the ice-free days are excluded. This focused approach ensures that the resulting statistics from both mean and 90th percentile values reflect active ice season conditions (typically spanning two to four months annually across the lakes). Inclusion of no-ice days would otherwise substantially reduce these values and compromise the representativeness of the ice season.

Fig. 9(a) maps the long-term average of annual maximum ice thickness from 1940 to 2022, computed by recording the peak thickness each year at every location and calculating their average over the study period (again, results for Lake Superior cover 1979-2022). The spatial ice thickness distribution reveals that thicker mean ice values are seen in the east basin of Lake Erie (up to 1.2 m), as well as the east and northeast side of Lake Huron (up to 0.8 m). In contrast, much thinner ice prevails in the central basins of all lakes, commonly below 0.4 m, with particularly low values (under 0.10 m) in central Lake Michigan and Lake Ontario. These patterns illustrate strong spatial variability driven by regional factors such as shallower bathymetry and/or colder localized climates in northern and coastal zones.

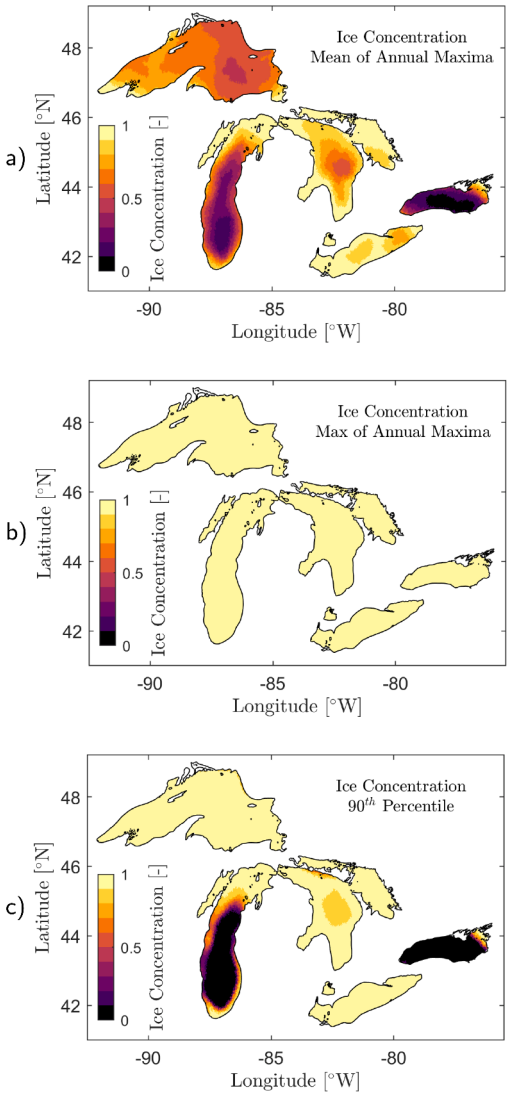

Fig. 8. Ice concentration results spanning the long-term period from 1940 to 2022. The plots illustrate: a) the mean of annual maxima, b) the max of annual maxima (extreme maximum), and c) the 90th percentile of ice concentration derived from the 83-year dataset.

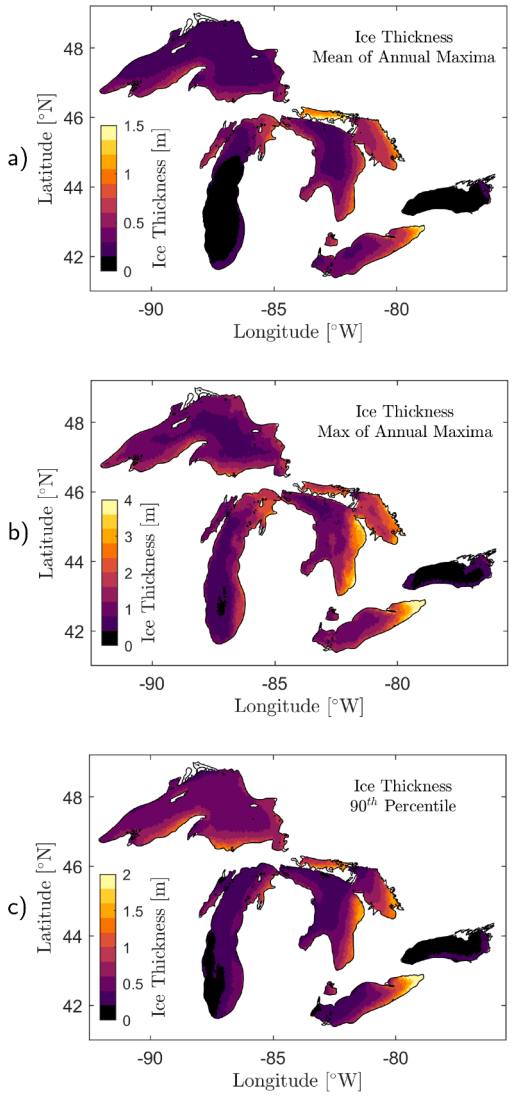

Fig. 9. Ice thickness results spanning the long-term period from 1940 to 2022. The plots illustrate: a) the mean of annual maxima, b) the max of annual maxima (extreme maximum), and c) the 90th percentile of ice thickness derived from the 83-year dataset.

The most extreme thickness values observed over the 83-year record are illustrated in Fig. 9(b). The thickest ice, up to around 4-4.5 m, develops in the eastern basin of Lake Erie along with the eastern regions of Lake Huron. This is consistent with some of the extreme ice thickness values reported by winter measurements in Lake Erie (Hawley et al., 2018). In contrast, Lake Ontario, central Lake Huron, and Lake Michigan's southern areas show far lower peak thicknesses.

Fig. 9(c) depicts the 90th percentile of ice thickness for the simulation period. This represents the ice thickness values that are exceeded only 10% to capture frequently high, but not most extreme ice conditions. The results indicate that ice thickness generally stays below 0.5 m in the central basins of Lakes Michigan and Huron, with significantly lower values at Lake Ontario. However, the 90th percentile ice thickness values may reach 1-2 m in eastern areas of Lake Erie and Lake Huron, as well as the coastal regions of Lake Superior.

3.4. Ice velocity

Ice velocity is another crucial parameter for the design and safety of offshore foundations, as the speed of ice motion can induce FLI and considerably amplify dynamic forces applied to platform structures and/or moorings. These forces impact both fatigue stresses and the structural resilience of infrastructure in regions prone to ice cover. To explore this, Fig. 10 presents the variability of ice velocity across the Great Lakes over the long-term study period. This analysis includes only days when ice concentration is at least 5% at each location and excludes the ice-free days. Otherwise, the no-ice days impose numerous zero-velocity values that could misrepresent actual ice dynamics by artificially lowering the computed means and 90th percentile values.

Fig. 10(a) displays the mean of annual maxima ice velocity values over the entire Great Lakes region. Peak mean velocities reach approximately 1 m/s in the Straits of Mackinac (the natural conduit connecting Lakes Michigan and Huron) and the western basin of Lake Erie. In contrast, persistently lower mean velocities are observed in Lake Ontario (under 0.2 m/s) and the southern section of Lake Michigan (typically under 0.3 m/s).

Additionally, extreme ice velocities recorded during the study period are visualized in Fig. 10(b), revealing substantial spatial variability. The highest maximum velocities, up to 1.5 m/s, are concentrated in

Lake Erie and the Straits of Mackinac, while Lake Ontario demonstrates comparatively modest peak velocities mostly below 0.5 m/s.

Finally, Fig. 10(c) illustrates the 90th percentile of ice velocity. These elevated ice velocities, which reflect the higher end of typical ice velocities, predominantly occur along the lakes' central axes. Interestingly, Lake Superior, Lake Erie, and the northeastern shores of Lake Huron (Georgian Bay) show reduced ice velocities near 0.25 m/s. On the other hand, deeper mid-lake zones of the other Great Lakes experience higher 90th percentile velocities, frequently nearing 0.4 m/s that highlights areas of increased dynamic ice activity.

Fig. 11 illustrates magnitude, distribution (frequency), and direction of ice velocity at two locations corresponding to the data and time period reported in Figs. 6 and 7. At Station 4a in Lake Erie (Fig. 11(a)), the longest spoke indicates that ice most frequently drifts toward the northeast direction, with typical speeds below 0.2–0.25 m/s in February 2011. At this period, only a very small fraction of the record reaches the highest speed of 0.35–0.4 m/s. At Station WM in Lake Superior (Fig. 11(b)), the distribution is relatively broader, but the dominant ice motion is oriented toward the northeast and east directions during February 2014. The color bands show that this site experiences relatively higher ice speeds with a noticeable portion of the record in the upper velocity bins and approaching velocities near 0.3–0.4 m/s.

4. Discussion on ice risks

As noted earlier, ice can impose multiple risks to the offshore wind turbines that operate in cold-climate regions. Some of these ice risks include the impact of drifting ice with tangible momentum on the platform, internal pressure generated by packed ice surrounding the structure, and icing on both the platform and turbine blades. In this section, some of these risks are further investigated and quantified for the Great Lakes region. The output can inform siting and engineering design of future offshore wind devices in this region to ensure the resiliency of these systems in the harsh winter. A case study is also carried out to further demonstrate the implementation of long-term hindcast data for estimating ice loads on the offshore platforms through common design standards.

4.1. Ice momentum

As drifting ice impacts an offshore wind structure, it exerts a large load on the platform and/or mooring systems. Besides the mechanical properties of ice (e.g., ice strength), this load is also dependent on some important factors such as ice concentration, thickness, and drifting velocity. To represent all these factors collectively, ice momentum can be taken into account. In general, the ice momentum can be expressed as:

$$M_{\text{ice}} = m_{\text{ice}}\ v_{\text{ice}} = (\rho\ A_{\text{ice}}\ h_{\text{ice}})\ v_{\text{ice}}, \tag{2}$$

where M_{ice} is the ice momentum, m_{ice} is the ice mass, v_{ice} is the ice drifting velocity, ρ is the ice density, A_{ice} is the area of the ice floe, and h_{ice} is the ice thickness. Based on FVCOM simulation data, the ice area at each cell can be written as:

$$A_{\text{ice}} = a_{\text{ice}}\ A_{\text{cell}}, \tag{3}$$

where a_{ice} is the fractional ice concentration and A_{cell} is the area of that cell. To remove the dependency of the momentum on the cell size of the computational domain, it is better to evaluate momentum per area. Using Eqs. (2) and (3), the ice momentum per area can be defined as follows:

$$M_{\text{ice}}/A_{\text{cell}} = \rho\ a_{\text{ice}}\ h_{\text{ice}}\ v_{\text{ice}}. \tag{4}$$

The momentum per area term clearly represents the contribution of important ice factors such as ice concentration, thickness, and velocity. Using Eq. (4), the momentum per area for the Great Lakes during the period of 1940-2022 is calculated and illustrated in Fig. 12.

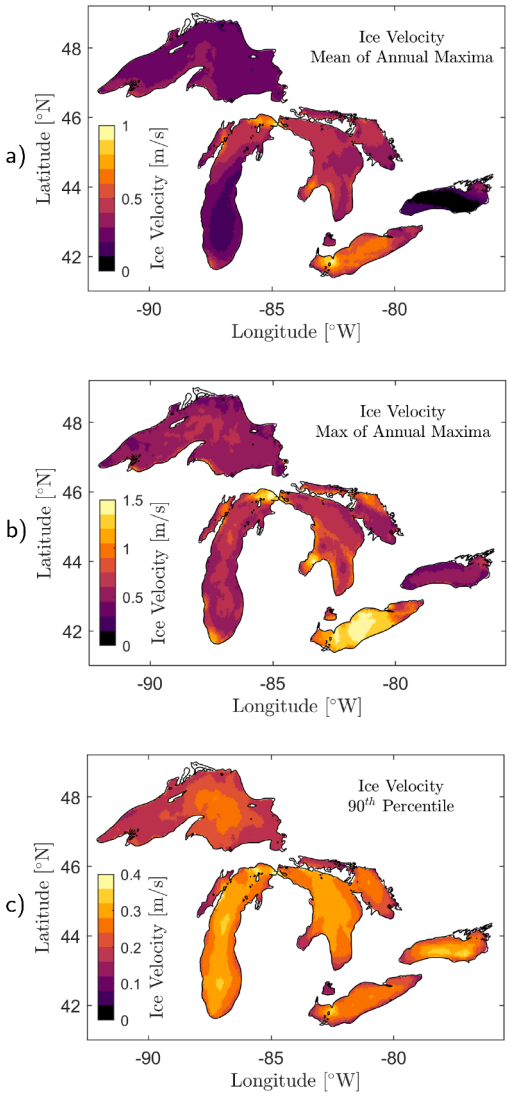

Fig. 10. Ice velocity results spanning the long-term period from 1940 to 2022. The plots illustrate: a) the mean of annual maxima, b) the max of annual maxima (extreme maximum), and c) the 90th percentile of ice velocity derived from the 83-year dataset.

Fig. 12(a) presents the mean momentum per area from all winters in the 83-year time period. Results show that Lake Erie and Lake Huron experience higher ice momentum compared with the other lakes, with estimates greater than 60 kg/(m.s) in near the eastern shores of both lakes. Even though high ice velocities have a major contribution in this, the higher ice thickness in these regions appears to play a more significant role in producing higher ice momentum (see Figs. 9(a) and 10(a)). On the contrary, significantly lower ice momentum values are observed for Lake Ontario and Lake Michigan. A similar pattern is observed for the 90th percentile values of ice momentum in winters (Fig. 12(b)). Again, higher ice momentum per area values of up to 146 kg/(m.s) are observed at the eastern regions of Lake Superior and Lake Huron.

It is worth noting that many regions, including central Lake Michigan, experience high ice velocity (Fig. 10(c)), but are classified as having relatively low ice momentum (Fig. 12(b)). This is because high ice velocities do not necessarily indicate challenging ice conditions if they are associated with thin (Fig. 9(c)) and low concentration (Fig. 8(c)) ice.

This section has focused on the magnitude of ice momentum as a key factor for initial siting and preliminary evaluation; however, ice momentum is inherently a vector quantity whose direction is aligned with

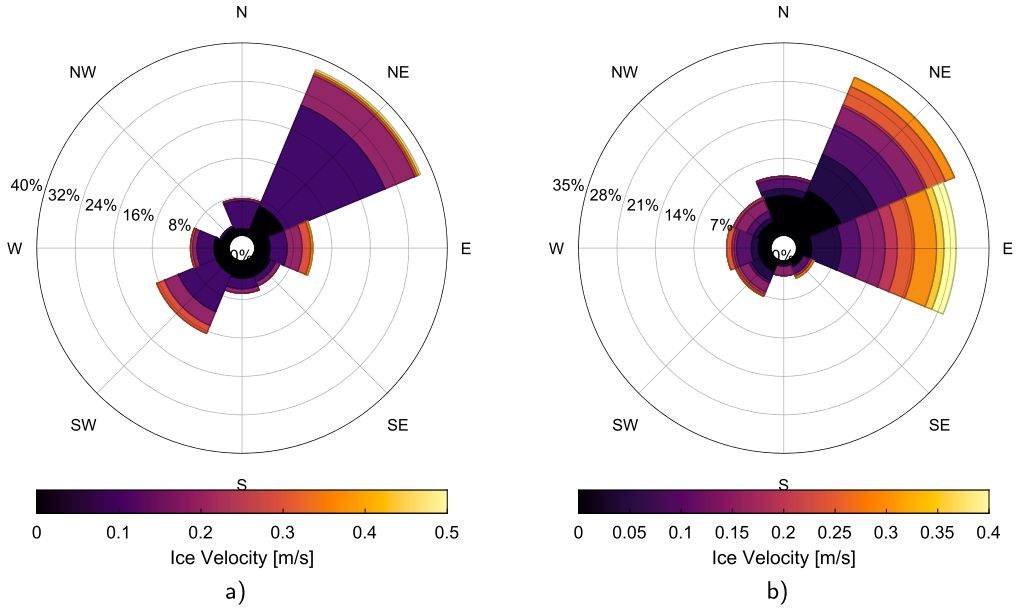

Fig. 11. Ice roses showing the magnitude, distribution (frequency), and direction of ice velocity at a) Station 4a in Lake Erie in February 2011 (corresponding to ice data presented in Fig. 6), and b) Station WM in Lake Superior in February 2014 (corresponding to ice data presented in Fig. 7). Each spoke around the circle indicates a direction toward which the ice is moving, and the length of each spoke, marked with radius percentages, indicates the percentage of time the ice moves in that direction. Colors on each spoke indicate the portion of time that ice moves within different velocity ranges.

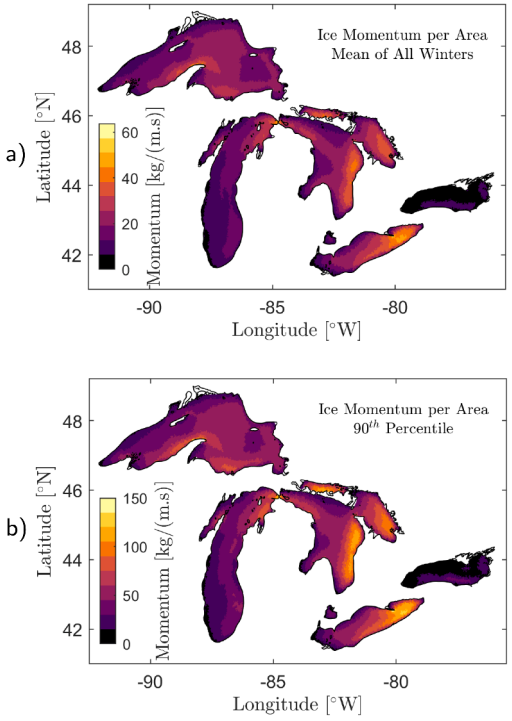

Fig. 12. Results of ice momentum per area for the long-term period of 1940-2022. Figures show a) mean values for all winters, and b) the 90th percentile of all the winters during the 83-year dataset.

the ice velocity direction (e.g., Fig. 11). For more detailed engineering tasks, such as the design of mooring systems and the layout and orientation of wind farm arrays, the full ice momentum vectors, including their directional variability and persistence, should be explicitly considered. This vector characterization should be investigated in conjunction with other environmental directionality parameters, such as wind, wave, and current directions.

4.2. Packed Ice

In addition to drifting ice impacting offshore wind structures, the formation of thick and static ice with high concentration (80–100%) can also impose significant loads on the system. This bonded and residual ice, hereafter referred to as “packed” ice (also known as “locked-in” ice), can exert prolonged pressure on foundations, causing bending and fatigue stresses as well as ice-induced vibrations. Such stresses continuously apply compressive forces on the platform and/or mooring systems. Moreover, the accumulation of ice around the structure and mooring lines will act as added mass, which poses risks to structural integrity and stability of the system. Packed ice conditions can also hinder winter inspection and maintenance activities. Therefore, it is critical to identify regions where packed ice forms and remains for extended durations each year.

Fig. 13 portrays the probability of ice formation exceeding 80% concentration for durations of five days or longer during the study period. In other words, this figure identifies the likelihood of locations experiencing packed ice for at least five days annually. As anticipated, Lake Erie exhibits the highest annual probability of packed ice occurrence with nearly 90-100% for most areas except the northeastern basin. Lake Huron also shows elevated probabilities, particularly in the southwestern area (Saginaw Bay) and northwestern region (Georgian Bay). Conversely, Lake Ontario, along with the southern and central portions of Lake Michigan, demonstrates the lowest probabilities of packed ice formation. These regions present promising candidates for offshore wind developments that seek sites with minimal packed ice risks.

4.3. Icing

Given the significant impact of icing on structural integrity and turbine performance, accurately assessing icing risk is essential to ensure the safe and efficient operation of offshore wind installations in cold regions such as the Great Lakes. In this study, the Overland icing algorithm is used to estimate and characterize icing in the Great Lakes (Overland, 1990; Overland and Spindler, 2025). Originally developed for 25–75 m vessels, which are comparable in size to offshore wind turbines, this model remains in use by the NOAA Ocean Prediction Center Ocean

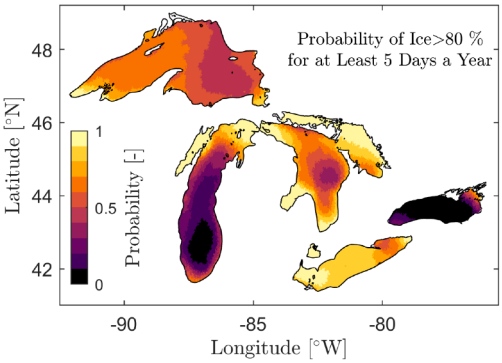

Fig. 13. Spatial distribution illustrating the probability of ice concentration more than 80% for at least 5 days a year. Results are shown for the 83-year dataset.

Table 1
Icing classes defined based on the icing predictor (IPR) calculated using the Overland (1990) icing algorithm.

	Icing class			
	Light	Moderate	Heavy	Extreme
IPR [$m°Cs^{-1}$]	<22.4	22.4–53.3	>53.3	>83.0

Applications Branch. The algorithm calculates icing predictors and rates based on air temperature, water temperature, and wind speed. Overland (1990) proposed the icing predictor as a method to estimate the likelihood of ice formation on exposed marine structures:

$$\text{IPR} = \frac{V_a\,(T_f - T_a)}{1 + 0.3\,(T_w - T_f)} \tag{5}$$

where IPR is icing predictor [$m°Cs^{-1}$], V_a is wind speed [m/s], T_f is the freezing temperature of water ($T_f = 0$ °C for fresh water), T_a and T_w are the air and water temperatures [°C], respectively. Once the icing predictor is computed, the icing class can then be identified via Table 1.

Fig. 14 illustrates the spatial distribution of icing potential across the Great Lakes, using the Overland (1990) icing predictor. Fig. 14(a) shows the icing predictor values averaged over all winters, while Fig. 14(b) illustrates 90th percentile (extreme event) values. The corresponding icing severity classes are also portrayed in Fig. 14(c) and (d), respectively.

Fig. 14(a) shows the mean icing predictor values across the Great Lakes, revealing a consistent north–south gradient with higher icing risk concentrated in northern Lake Superior, northern Lake Michigan, and north-eastern Lake Huron. Conversely, southern areas including southern Lake Michigan, Lake Erie and Lake Ontario experience lower icing values. Fig. 14(b) displays the 90th percentile icing predictor, highlighting these same northern regions as most susceptible to severe icing during extreme winter events, with values exceeding 100 $m°Cs^{-1}$. This pattern indicates that elevated icing risk in the north is present both on mean and 90th values and intensifies during peak winter events.

The ice class maps depicted in Fig. 14(c) and (d) reinforce these patterns. Under average winter conditions, Fig. 14(c), much of the northern lakes experience moderate icing, while the southern lakes see mostly light icing. However, during extreme events (Fig. 14(d)), heavy and even extreme icing becomes prevalent in northern and central sectors. This figure shows that Lake Ontario and central to southern Lake Michigan are more ideal sites to avoid heavy and extreme icing during extreme events.

Additionally, Overland (1990) developed an algorithm to estimate the icing rate based on the icing predictor through a cubic polynomial fit:

$$\text{Icing Rate [cm/h]} = A\,(\text{IPR}) + B\,(\text{IPR})^2 + C\,(\text{IPR})^3, \tag{6}$$

where $A = 2.73 \times 10^{-2}$, $B = 2.91 \times 10^{-4}$, and $C = 1.84 \times 10^{-6}$ are the cubic polynomial fit parameters. While these parameters were developed for the Alaskan waters, the Overland algorithm (Eqs. (5)–(6)) can also be used for the Great Lakes by adjusting the freezing temperature ($T_f = 0$ °C) as suggested by Guest and Luke (2005).

Fig. 15 depicts the spatial distribution of the mean and 90th percentile values of icing rate during the winters of the study period. Similar to the icing predictor figures, higher icing rates are concentrated in northern Lake Superior, northern Lake Michigan, and parts of north-eastern Lake Huron. These values exceed 2 cm/h for mean icing rate (Fig. 15(a)) and 8 cm/h for the 90th percentile (extreme event) values (Fig. 15(b)). Again, Lake Ontario, central and southern Lake Michigan, and Lake Erie experience lower icing rates relative to other regions.

It is worth mentioning that further atmospheric and marine parameters (e.g., relative humidity, surface pressure, wind direction, significant wave height, cold soaking) and turbine-specific details (e.g., height above the waterline, structure materials, surface) can be considered for more accurate icing estimations. However, these additional parameters are found to be generally of second- and third-order effects (Overland and Spindler, 2025). Since Overland algorithm covers the main and first-order effects, it prioritizes simplicity for operational marine meteorological applications, as it remains in operational use by the U.S. and other countries (Overland and Spindler, 2025).

These results emphasize the icing risk across the Great Lakes and underscore the necessity for site-specific assessments of severe and persistent icing during offshore wind turbine planning. High-risk areas identified in this analysis may necessitate enhanced mitigation strategies, including specialized turbine designs, advanced anti-icing and de-icing technologies, and increased maintenance protocols.

4.4. Ice intensity

In previous sections, the ice momentum, packed ice, and icing risks were evaluated. To more comprehensively assess the risks posed by lake ice to offshore wind infrastructure, we introduce the concept of ice intensity, which synthesizes multiple independent factors into a single metric. The ice intensity index is formulated as a weighted sum of three key parameters:

$$\text{Ice Intensity} = R_{\text{M}}\,W_{\text{M}} + R_{\text{I}}\,W_{\text{I}} + R_{\text{P}}\,W_{\text{P}}, \tag{7}$$

where R_{M} is the ice momentum risk, R_{I} is the icing risk, and R_{P} is the packed ice risk. The ice momentum and icing risks are obtained by non-dimensionalizing the spatial distribution of ice momentum per unit area (Fig. 12(a)) and icing predictor (Fig. 14(a)) with respect to their corresponding maximum values to yield normalized measures between 0 and 1. The packed ice risk, R_{P}, is taken directly from the packed ice probability distribution (Fig. 13). The associated weighting factors W_{M}, W_{I}, and W_{P} correspond to the relative importance of ice momentum, icing, and packed ice probabilities, respectively. The weighting factors should be determined by designers based on the platform's specific design, ice-structure interaction characteristics, and operational requirements at the target site. This is to ensure that the ice intensity index accurately reflects the unique conditions and risk priorities relevant to each project. For example, floating platforms may face greater consequences from icing than fixed structures, as ice accumulation elevates the waterline, induces additional loading on the mooring lines, compromises platform's stability, and restricts turbine operations within safe operational envelopes. Consequently, designers may assign a higher weighting factor to icing risk (W_I) for floating platforms to properly account for these amplified loads and critical conditions.

Fig. 16 presents the spatial distribution of the mean ice intensity index across the Great Lakes, integrating the combined effects of icing, ice momentum, and packed ice conditions. For this figure, it is assumed $W_{\text{M}} = W_{\text{I}} = W_{\text{P}} = 0.33$. The equal weighting in this figure is deliberately chosen as a first order approximation that treats all three hazard mechanisms as equally important without subjective prioritization. The map

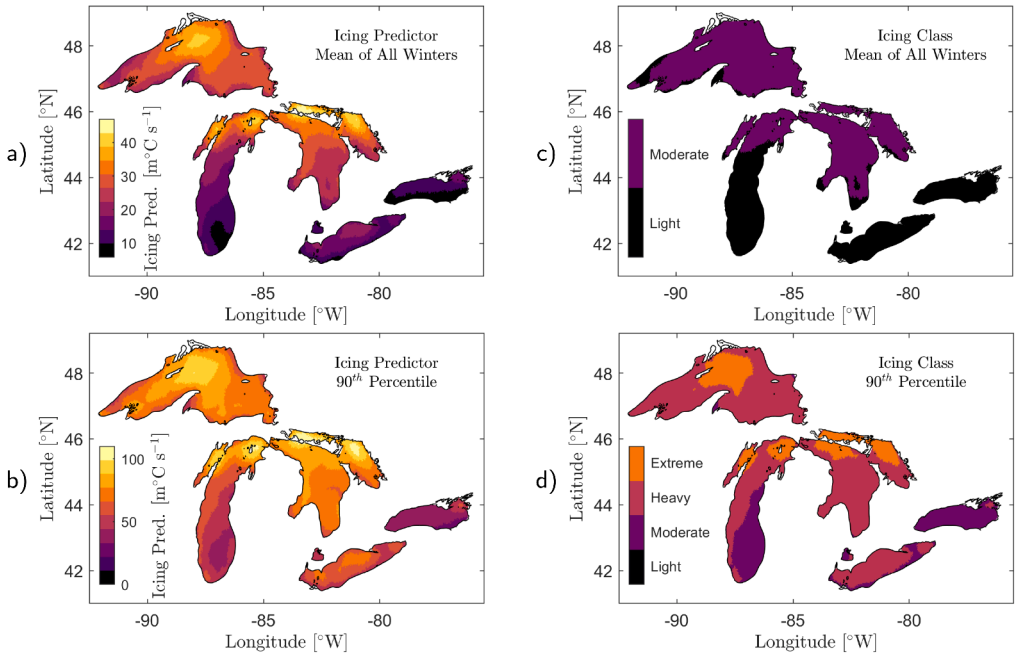

Fig. 14. Icing predictor and class for the Great Lakes. Figures illustrate a) mean of icing predictor for all winters, b) 90th percentile icing predictor for all winters, c) icing class for mean of all winters, and d) icing class for the 90th values. The icing predictor and class are calculated based on Overland (1990).

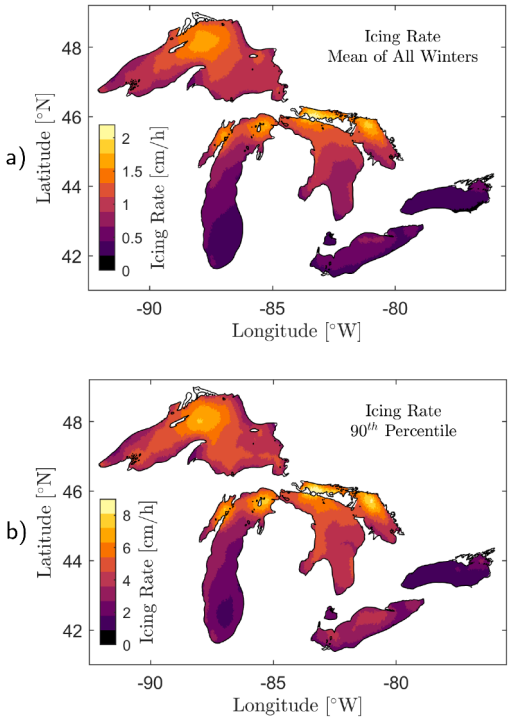

Fig. 15. Icing rate for the long-term period of 1940-2022. Figures show a) mean values for all winters, and b) the 90th percentile for the winters of the 83-year dataset.

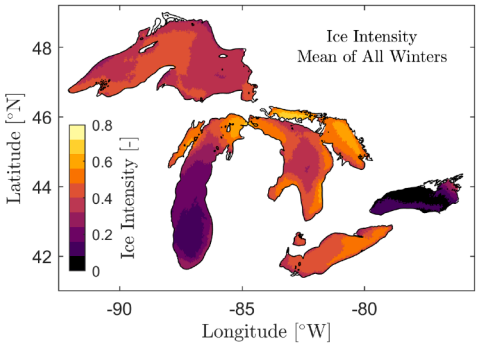

Fig. 16. Spatial distribution of the mean ice intensity index across the Great Lakes, illustrating the combined effects of icing, ice momentum, and packed ice. Lower index values highlight regions with smaller overall ice-related hazards. This is a generic risk indicator obtained by treating all three hazard mechanisms as equally important ($W_M = W_I = W_P = 0.33$) without subjective platform prioritization.

reveals that northern regions of Lakes Michigan, Huron, Erie, and Superior exhibit higher mean ice intensity values (~0.8), indicating persistent and significant ice-related challenges in these locations. In contrast, Lake Ontario as well as central and southern Lake Michigan regions generally experience much lower ice intensity, reflecting reduced combined ice hazards. This spatial pattern demonstrates how the ice intensity metric effectively captures the aggregate risk landscape for offshore wind development. It also enables more informed decisions regarding site selection and risk mitigation in the Great Lakes region. As noted earlier, more comprehensive work is needed to obtain the weighting parameters for specific platform types, geometries, and dynamic characteristics, as well as their intended operational envelopes. Such tailoring would yield an ice intensity map explicitly optimized for the target design, rather than a generic risk indicator as shown in Fig. 16. This approach facilitates a more holistic evaluation of site suitability and risk, capturing not only the direct impact of surface icing but also the structural challenges posed by prolonged ice coverage and the mechanical forces of drifting ice. Such a comprehensive metric is particularly valuable in the Great Lakes, where the interplay of these ice phenomena can be highly variable and have significant implications for the design, siting, and long-term resilience of offshore wind developments.

4.5. Overall characteristics

Table 2 provides a comprehensive summary of key ice conditions in the Great Lakes, reporting mean annual maxima, absolute maximum,

Table 2
Summary of the Great Lakes ice conditions for two different periods: 1940–2022, and 1979–2022. The Mean of annual maximum, Max of annual maximum (absolute maximum), and 90th percentile values are reported for ice cover, thickness, and velocity. Mean and 90th percentile values correspond to averaged quantities for each lake during winter seasons of the selected period.

	Period 1940–2022								
	Ice Cover [%]			Ice Thickness [m]			Ice Velocity [m/s]		
Lake	Mean of Annual Max	Max of Annual Max	90^{th} Percentile	Mean of Annual Max	Max of Annual Max	90^{th} Percentile	Mean of Annual Max	Max of Annual Max	90^{th} Percentile
Superior	–	–	–	–	–	–	–	–	–
Michigan	60	100	50	0.25	3.19	0.36	0.32	1.41	0.27
Huron	87	100	95	0.56	5.45	0.64	0.42	1.42	0.26
Erie	90	100	99	0.55	4.83	0.72	0.55	1.40	0.24
Ontario	27	100	10	0.05	1.57	0.16	0.12	0.85	0.26
	Period 1979–2022								
	Ice Cover [%]			Ice Thickness [m]			Ice Velocity [m/s]		
Lake	Mean of Annual Max	Max of Annual Max	90^{th} Percentile	Mean of Annual Max	Max of Annual Max	90^{th} Percentile	Mean of Annual Max	Max of Annual Max	90^{th} Percentile
Superior	65	100	98	0.32	4.52	0.62	0.27	1.29	0.20
Michigan	53	100	40	0.21	3.19	0.33	0.29	1.41	0.27
Huron	82	100	93	0.49	4.63	0.64	0.40	1.40	0.26
Erie	86	100	99	0.47	3.96	0.68	0.51	1.39	0.24
Ontario	23	100	7	0.04	1.44	0.16	0.10	0.72	0.26

Table 3
Ice properties used in the case study. These parameters mainly represent the IceFloe (Mccoy et al., 2014) benchmark study condition, with the key enhancement of implementing time-varying and dynamic ice thickness derived directly from FVCOM simulations.

Property	Great Lakes A	This Study
Ice thickness [m]	1	Dynamic
Reference strength [MPa]	2.2	2.2
Flexural strength [MPa]	0.7	0.7
Elastic modulus [GPa]	8.0	8.0
Poisson ratio [–]	0.3	0.3
Ice-to-ice friction coefficient [–]	0.05	0.05
Water density [kg/m^3]	999.8	999.8
Ice density [kg/m^3]	916.2	916.2
Angle of the ice rubble [deg]	40	40
Porosity of the ice rubble [–]	0.3	0.3
Cohesion of the ice rubble [Pa]	0	0
Friction angle of the ice rubble [deg]	45	45
Ride-up thickness[a] [m]	2.5	Dynamic
Korzhavin contact factor [–]	0.5	0.5

[a] Ride-up thickness is set as 2.5 times the ice thickness.

Table 4
Characteristics of the offshore wind platform used in this case study, configured to match the full-scale IceFloe benchmark platform (Mccoy et al., 2014).

Property	Value
Diameter/width [m]	14.2
Cone angle [deg]	52.0
Ride-up (rubble) height [m]	4.0
Top diameter of tower cone [m]	8.0
Ice-to-structure friction coefficient [–]	0.15
Korzhavin shape factor [–]	0.9

Table 5
Ice limit load values calculated by this study compared with the IceFloe benchmark results (Mccoy et al., 2014) for the test condition Great Lakes A (see Table 3). Consistent with the IceFloe condition, the ice thickness for the representative platform is set to 1 m for the calculation.

Limit Load	Calculation	IceFloe
ISO Crushing [MN]	20.433	20.433
IEC Crushing [MN]	16.347	16.347
ISO Flexural [MN]	3.374	3.376
IEC Flexural [MN]	5.044	5.045

and 90th percentile values for ice cover, thickness, and velocity over two periods: 1940–2022 and 1979–2022. Mean and 90th percentile values correspond to averaged quantities for each lake during winter seasons of the selected period. This table captures both typical and extreme scenarios and highlights substantial spatial variability over different lakes.

Such synthesized statistics are critical for contextualizing ice hazards in offshore wind development, supporting nuanced assessments of both average conditions as well as rare and high-intensity events. These metrics are particularly valuable in the pre-design and conceptual stages to help stakeholders identify site-specific risks and inform the development of initial design requirements.

4.6. Case study

To demonstrate the practical utility of the reported long-term ice hindcast for offshore wind design, a case study is conducted that applies the simulated results to quantify design-basis ice loads on a representative platform. This case study illustrates a transferable methodology applicable to arbitrary offshore wind sites across the Great Lakes.

4.6.1. Test configuration

The ice properties adopted in the case study are summarized in Table 3. These parameters are selected to closely reproduce the “Great Lakes A” condition from the IceFloe benchmark study (Mccoy et al., 2014). IceFloe is a dedicated module within the OpenFAST wind turbine multiphysics framework that computes ice floe loads on fixed offshore structures. The main enhancement in this study is that the ice thickness is treated as a time-varying and dynamic variable derived directly from the FVCOM simulations. Additionally, Table 4 summarizes the characteristics of the representative offshore wind platform, configured to match the full-scale benchmark platform in the IceFloe (Mccoy et al., 2014). This selection also enables direct validation of computed ice loads against IceFloe predictions.

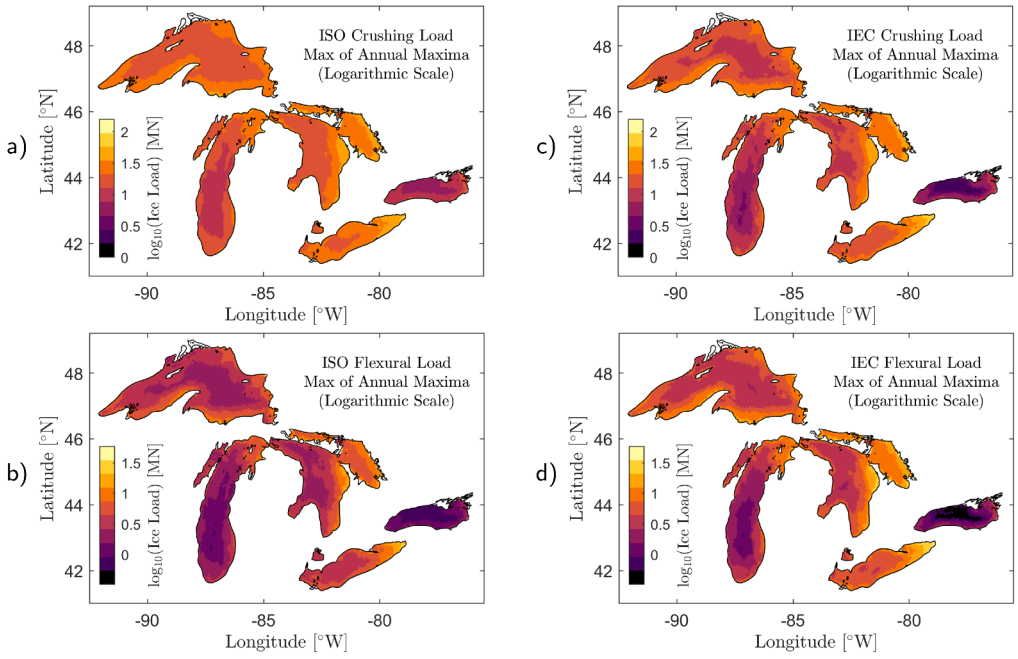

Fig. 17. Maximum ice loading based on ISO and IEC standards for the Great Lakes during 1979-2022. Figures demonstrate a) ISO limit crushing load, b) ISO limit flexural load, c) IEC limit crushing load, and d) IEC limit flexural load. The loads are calculated using maximum ice thickness for each location and results are presented on logarithmic scales to enhance visual clarity. For ice conditions and platform's characteristics, please refer to Tables 3 and 4, respectively.

4.6.2. Ice load models

Several established ice load models are applied in this study to translate hindcast ice data into design loads for the representative ice condition and platform. These models, widely adopted in offshore engineering standards of ISO 19906 (2010) and IEC 61400-3 (2009), include ISO crushing limit, IEC crushing limit, ISO flexural limit, and IEC flexural limit. These limit ice loads are selected to evaluate the primary failure modes of ice against offshore structures through crushing failure (limited by ice strength) and flexural failure (limited by bending strength). For crushing failure, level ice fails against the vertical structure face, where ice compressive strength directly governs the load magnitude (top-left case in Fig. 1(b)). Thus, a vertical-sided platform with no cone is assumed to evaluate the ice crushing failure. On the other hand, flexural failure occurs when ice bending strength limits the load, typically under a sloped/conical structure that induces beam failure at the ice edge (top-middle and top-right cases in Fig. 1(b)). As such, we choose to analyze a conical platform to assess the ice flexural failure. By enveloping global crushing and flexural limits, these ice models provide upper-bound loads essential for ensuring structural integrity under extreme Great Lakes ice events. Full formulations for all these models are detailed in Appendix A.

4.6.3. Ice load limits

Table 5 shows a comparison between calculated results for the ISO and IEC limit loads with those predicted from the IceFloe (Mccoy et al., 2014). In this case, the ice thickness encountering the representative platform is set to 1 m for the calculation to match the test condition of the IceFloe (Great Lakes A). The results successfully reproduce the IceFloe limit loads and confirm the validity of utilized ice parameters and load formulations.

Once the framework is verified, hindcast-driven ice thickness values can be used as the input to estimate the limit loads for the entire Great Lakes under harsh weather conditions during 1979-2022. Fig. 17 illustrates the maximum ISO and IEC crushing and flexural ice loading under max of annual maxima ice thickness (Fig. 9(b)) for the entire domain. To enhance visual clarity, results are presented on logarithmic scales. Since the main input is ice thickness, the limit ice load patterns look similar

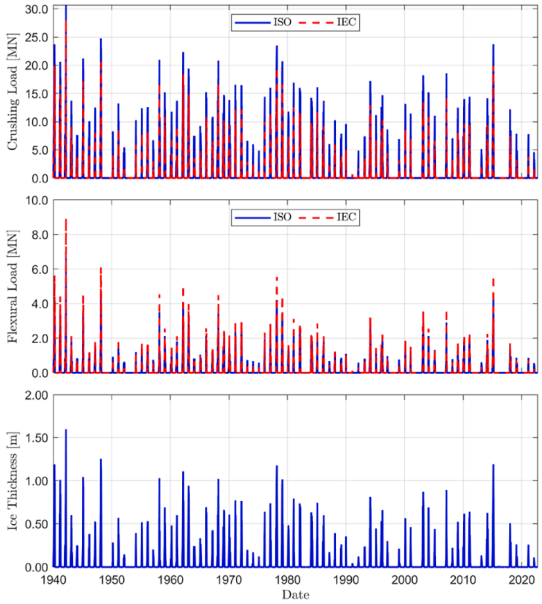

Fig. 18. Dynamic ice loads during 1940-2022 at Station 4a in Lake Erie (see Fig. 2). The ISO and IEC crushing and flexural loads are plotted, along with the variable ice thickness at this location.

under different ice limit models. However, different ice models result in different limit load values. It can be seen that crushing limit failures (17(a) and 17(c)) yield higher ice load values compared to the flexural limit failures (17(b) and 17(d)). For instance, maximum ISO crushing load for Lake Michigan is recorded at 55.41 MN, while the maximum ISO flexural load of 20.16 MN is computed at this lake for the period of 1979-2022. This difference mainly stems from the fact that the ice reference crushing strength (2.2 MPa, see Table 3) is substantially higher than the ice flexural strength (0.7 MPa). Consequently, offshore platforms in ice-prone regions are often equipped with an ice cone near

Table 6
Summary of the Great Lakes ice loads for two different periods: 1940–2022, and 1979–2022. The max of annual maxima (absolute maximum) values for ice loads are reported for each lake during winter seasons of the selected period. These values represent the worst-case scenario in each lake and not the design ice load values associated with plausible offshore wind sites.

Lake	Period 1940–2022				
	Max Ice Thickness [m]	ISO Crushing Load [MN]	IEC Crushing Load [MN]	ISO Flexural Load [MN]	IEC Flexural Load [MN]
Superior	–	–	–	–	–
Michigan	3.19	55.41	65.34	20.16	30.91
Huron	5.45	87.83	130.9	52.09	78.25
Erie	4.83	79.17	111.6	41.85	63.18
Ontario	1.57	30.12	27.50	6.40	9.87
Lake	Period 1979–2022				
	Max Ice Thickness [m]	ISO Crushing Load [MN]	IEC Crushing Load [MN]	ISO Flexural Load [MN]	IEC Flexural Load [MN]
Superior	4.52	74.78	102.3	37.15	56.24
Michigan	3.19	55.41	65.34	20.16	30.91
Huron	4.63	76.33	105.6	38.79	58.66
Erie	3.96	66.74	86.14	29.37	44.69
Ontario	1.44	27.96	24.85	5.63	8.65

the waterline, which shifts the governing failure mode from crushing to flexural and can drastically reduce the corresponding impact loads (Javaherian et al., 2025b; Shi et al., 2023).

Maximum ice load values for different lakes from different ice models are summarized in Table 6 for two periods of 1940-2022 and 1979-2022. These values reflect the worst-case scenario in each lake that usually occurs in nearshore and shallow regions. Although such ice loads are not representative of conditions at plausible offshore wind sites, they are included to provide a reference for the maximum potential ice loads in each lake. As far as the flexural limit loads are concerned, IEC load limits are generally about 50% higher than those from the ISO model for the presented ice thickness range. This difference, mainly coming from the assumptions and factors in these models, reveals that IEC model permits significantly larger ice-induced bending loads before reaching the design limit. Hence, using IEC flexural values would generally lead to a more conservative (heavier and more robust) structure, because members and foundations must be sized to resist higher characteristic ice loads. Conversely, using ISO flexural limits would allow a more economical design but with lower implied safety margin against flexural ice failure. This difference is important to highlight, especially for sites where flexural failure dominates, since the choice of standard directly controls the governing ultimate limit state and thus the overall structural sizing and costs.

The simulated time-varying and dynamic ice characteristics also enable estimating dynamic ice loads at specific target sites. Fig. 18 illustrates an example of the dynamic ISO and IEC limit loads at Station 4a in Lake Erie (see Fig. 2). In this figure, the dynamic ice thickness for the period of 1940-2022 is shown along with the ISO and IEC flexural and crushing limit loads. Results show that the maximum ice limit load at this station was recorded on 7th March 1942, resulting from an ice thickness of 1.6 m. At this time, maximum ice loads of 30.65 MN and 28.17 MN are recorded based on the ISO and IEC crushing limits, respectively. Again, these values are significantly higher than the flexural limit loads, which are 6.60 MN for ISO flexural load and 8.94 MN for IEC flexural load. Additionally, for this range of ice thickness (0-1.6 m), the ISO crushing limit loads tend to be higher than IEC crushing limits. However, as was shown in Table 6, this is not a general trend for other ice thicknesses.

It is worth noting that more comprehensive dynamic ice load models can be explored that account for additional ice characteristics such as ice concentration and velocity (e.g., Määttänen (1998) ice crushing dynamics). Further analysis can be conducted to determine the return period of the design ice load at the target site. However, this case study suffices to employ the ISO/IEC limit loads, the primary design-based approach in offshore engineering practice, to demonstrate the practical utility of our hindcast dataset for rapid and early-stage ice load estimation.

5. Conclusions and future work

This study presents a thorough assessment of ice-related risks for offshore wind development in the Laurentian Great Lakes by leveraging an advanced hydrodynamic-ice modeling framework, namely FVCOM–CICE. By generating an 83-year hindcast of lake ice dynamics including concentration, thickness, and velocity, this work addresses critical data and knowledge gaps that have historically hindered the engineering and siting of offshore wind developments in this region.

Model validation against satellite and in-situ observations confirms the reliability of simulated ice metrics for pre-design applications. Key insights from this study highlight marked spatial patterns and variability in ice characteristics across the Great Lakes. Regions such as Lake Erie, Lake Huron, and portions of Lake Superior are characterized by persistent and significant ice cover, thicker ice, and higher velocities. In contrast, Lake Ontario as well as central and southern Lake Michigan regions typically experience lower ice concentrations and thickness. Also, mean of annual maxima, max of annual maxima, and 90th percentile values for ice cover, thickness, and velocity were quantified and reported for different lakes.

Additionally, this study introduces a composite ice intensity index by synthesizing mechanical and environmental ice hazards such as ice momentum, packed ice pressure, and icing severity. The spatial mapping of the ice intensity index enables a more holistic evaluation of regional ice risks relevant to offshore wind engineering. Not only does this unified hazard metric facilitate the identification of promising sites for development with minimized ice impacts, but also supports the development of relevant design criteria, advanced de-icing and anti-icing strategies, and maintenance protocols that are tailored to the severity of local ice regimes. Furthermore, a case study is presented to highlight practical applications of the hindcast data. The hindcast ice thickness data were directly input into ISO/IEC limit ice load models to quantify design loads for representative offshore wind platforms.

The Great Lakes exhibit relatively short ice seasons but locally much thicker ice, with extreme ice thicknesses reaching about 4–5 m in some basins. In contrast, many European cold-climate waters, particularly in the Baltic Sea and its northern sub-basins such as the Bay of Bothnia,

experience more persistent seasonal ice that is generally thinner, with typical design level-ice thicknesses of about 1 m (Tikanmäki et al., 2025). As noted earlier, freshwater ice is mechanically stronger than sea ice due to lower brine volume (Weeks and Ackley, 1986). Therefore, Great Lakes ice implies higher potential ice loads compared to Baltic Sea ice for a given thickness.

It is worthwhile to mention that global warming has substantially reduced the Great Lakes ice cover (e.g., declining about 70% from 1973–2010; Wang et al. (2012)). However, 80-year projections still indicate that persistent ice cover will be observed through 2100 and will not fully disappear (Xue et al., 2022). On the other hand, recent findings show that climate change is simultaneously amplifying temperature extremes and variability. For instance, cold-spells at the Great Lakes are observed to be increased by +1 day per year (Abdelhady et al., 2025a). These prolonged thermal extremes, driven by Arctic amplification and polar vortex destabilization, sustain the potential for severe ice loading events despite declining mean ice cover (Abdelhady et al., 2025a,b). Therefore, as ice risks will remain an important design criterion for long-term offshore and near-shore infrastructure planning, these non-linear shifts need to be considered for ice loading estimations under increasing climate uncertainty.

Looking forward, integrating these ice hazard characterizations with other site-specific environmental, economic, and logistical factors will further strengthen multi-criteria decision frameworks for offshore wind development in this region. Continuous improvement in ice modeling and expanded observational datasets will further refine risk assessments and support safe, efficient, and cost-effective renewable energy infrastructure amid a changing climate in this freshwater environment.

Overall, this study establishes a rigorous foundation for the engineering design and planning of offshore wind developments in the Great Lakes. The quantitative hazard maps and metrics serve as critical guidance for selecting optimal sites, designing robust structures, and formulating operational strategies to ensure safe and efficient wind energy development in this region.

CRediT authorship contribution statement

M. Javad Javaherian: Writing – review & editing, Writing – original draft, Visualization, Validation, Methodology, Investigation, Formal analysis, Data curation, Conceptualization; **Hazem Abdelhady:** Writing – review & editing, Writing – original draft, Methodology, Data curation, Conceptualization; **David Cannon:** Writing – review & editing, Writing – original draft, Supervision, Software, Resources, Project administration, Methodology, Funding acquisition; **Jia Wang:** Supervision, Resources, Funding acquisition; **Ayumi Fujisaki-Manome:** Writing – review & editing, Writing – original draft, Supervision, Software, Resources, Project administration, Methodology, Funding acquisition; **Lei Zuo:** Writing – review & editing, Writing – original draft, Supervision, Resources, Project administration, Funding acquisition, Conceptualization.

Declaration of competing interest

The authors declare that they have no known competing financial interests or personal relationships that could have appeared to influence the work reported in this paper.

Acknowledgment

The authors gratefully acknowledge the support from the NOAA OAR Ocean Sciences Portfolio for the Great Lakes Earth System Model (GLESM) project, the Great Lakes Environmental Research Laboratory for the Ice Studies project, and the NOAA GOMO Arctic Research Program for the Arctic Forecast System project. Furthermore, HUA, DC, and AFM were also supported by the National Science Foundation (NSF OCE 2319044). This is GLERL contribution #2094 and CIGLR contribution #1277.

Appendix A. Ice Load Models

Several established ice load models are presented here. These models include current ISO and IEC standards for ice crushing and ice flexural failure modes.

A.1. ISO limit crushing

The ISO 19906 (2010) standard defines the global limit load for ice crushing through empirical corrections applied to a reference ice strength. The ISO ice crushing limit load, P, is given by:

$$P = p_G h w. \tag{A.1}$$

where p_G is the global average ice pressure [MPa], w is the projected width of the structure [m], and h is the ice thickness [m]. The global average ice pressure is calculated as:

$$p_G = C_R \left(\frac{w}{h}\right)^m \left(\frac{h}{h_1}\right)^n \tag{A.2}$$

where C_R is the ice reference strength [MPa] determined by ice regime and environmental severity (ranging from 1 MPa to 3 MPa; the standard specifies 2.8 MPa for the Beaufort Sea and 1.8 MPa for the Baltic Sea), $h_1 = 1.0$ m is the reference ice thickness, and $m = -0.16$ is an empirical constant. The exponent n depends on ice thickness:

$$n = \begin{cases} -0.5 + h/5 & h < 1.0 \text{ m} \\ -0.3 & h > 1.0 \text{ m} \end{cases} \tag{A.3}$$

This formulation accounts for scale effects and aspect ratio and is supported by extensive field measurements.

A.2. IEC limit crushing

The IEC 61400-3 (2009) recommends the Korzhavin equation for calculating the limit force, P, from ice crushing on vertical structures:

$$P = k_1 k_2 k_3 h w \sigma_c \tag{A.4}$$

where w and h represent the projected width and ice thickness, respectively, and σ_c is the ice crushing strength [MPa]. The coefficients k_1, k_2, and k_3 adjust for structure shape, contact conditions, and aspect ratio. The shape factor k_1 is defined as:

$$k_1 = \begin{cases} 1.0 & \text{for rectangular shapes} \\ 0.9 & \text{for circular shapes} \end{cases} \tag{A.5}$$

The contact factor k_2 is:

$$k_2 = \begin{cases} 0.5 & \text{for moving ice} \\ 1.0 & \text{for frozen ice} \\ 1.5 & \text{for locally thickened ice} \end{cases} \tag{A.6}$$

The aspect ratio factor k_3 follows:

$$k_3 = \sqrt{1 + 5\frac{h}{w}} \tag{A.7}$$

When local data are unavailable, typical crushing strengths σ_c include 3.0 MPa for cold moving ice or 1.5 MPa for spring ice near melting.

A.3. ISO limit flexural

For wide slopes or conical structures, flexural failure can be analyzed by treating the ice sheet as an elastic beam on an elastic foundation, incorporating 3D effects and rubble presence. This approach applies to downward-breaking slopes by substituting ice buoyancy for air weight. The total horizontal force from this model, F_H, is:

$$F_H = f(H_B + H_P + H_R + H_L + H_T) \tag{A.8}$$

where H_B is breaking load, H_P pushes ice through rubble, H_R pushes ice blocks up slope, H_L lifts rubble, and H_T turns the ice block. The breaking component is:

$$L_c = \left(\frac{E h^3}{12\,\rho_w\, g\,(1-\nu^2)} \right)^{0.25} \tag{A.9}$$

and

$$\xi = \frac{\sin\alpha + \mu_s \cos\alpha}{\cos\alpha - \mu_s \sin\alpha} \tag{A.10}$$

where α is the slope angle of the structure, μ_s is the coefficient of friction between ice and structure, σ_f is the flexural strength of the ice, ρ_w is the density of water, E is the elastic modulus of ice, and ν is the Poisson's ratio for ice.

The breaking load, H_B, can then be calculated as:

$$H_B = 0.68\,\xi\,\sigma_f \left[w + \pi^2 \frac{L_c}{4} \right] \left[\frac{\rho_w g h^5}{E} \right]^{0.25}. \tag{A.11}$$

The rubble push-through load is:

$$H_P = \frac{w\, h_r^2\, \mu_i\, \rho_i\, g\,(1-e)(1-\tan\theta/\tan\alpha)^2}{2\tan\theta}, \tag{A.12}$$

where h_r is the height of the rubble, μ_i is the ice-to-ice coefficient of friction, e is the porosity of the rubble, θ is the angle the rubble pile makes with the horizontal, and ρ_i is the density of the ice.

The effective the weight of the rubble pile, P, can then be calculated as:

$$\begin{aligned} P = {} & 0.5\,\mu_i\,(\mu_i+\mu_s)\,\rho_i\,g\,(1-e)\,h_r^2\,\sin\alpha\left(\frac{1}{\tan\theta}-\frac{1}{\tan\alpha}\right)(1-\tan\theta/\tan\alpha) \\ & + 0.5\,(\mu_i+\mu_s)\,\rho_i\,g\,(1-e)\,h_r^2\,\frac{\cos\alpha}{\tan\alpha}(1-\tan\theta/\tan\alpha) + h_r\,h\,\rho_i\,g\left(\frac{\sin\alpha+\mu_s\cos\alpha}{\sin\alpha}\right) \end{aligned} \tag{A.13}$$

Then, H_R, the load that is required to push the ice floes through the rubble and on the slope of the structure can be computed:

$$H_R = \frac{wP}{\cos\alpha - \mu_s \sin\alpha}. \tag{A.14}$$

Additionally, the rubble lift load is:

$$\begin{aligned} H_L = {} & 0.5\,w\,h_r^2\,\rho_i\,g\,(1-e)\,\xi\left(\frac{1}{\tan\theta}-\frac{1}{\tan\alpha}\right)(1-\tan\theta/\tan\alpha) \\ & + 0.5\,w\,h_r^2\,\rho_i\,g\,(1-e)\,\xi\,\tan\phi\,(1-\tan\theta/\tan\alpha)^2 + \xi\,c\,w\,h_r\,(1-\tan\theta/\tan\alpha) \end{aligned} \tag{A.15}$$

where c is the cohesive strength of the ice rubble, ϕ is the friction angle of the ice rubble.

Finally, H_T represents the force required to turn the ice blocks at the interface between the conical and upper cylindrical sections of the structure:

$$H_T = 1.5\,w\,h^2\,\rho_i\,g\left(\frac{\cos\alpha}{\sin\alpha - \mu_s\cos\alpha}\right) \tag{A.16}$$

ISO 19906 recommends modifying the flexural strength of the ice sheet to account for the pre-stress effect of in-plane forces. Thus:

$$F_H = \frac{H_B + H_P + H_R + H_L + H_T}{1 - \frac{H_B}{h\,l_c\,\sigma_f}} \tag{A.17}$$

where

$$l_c = w + \frac{\pi^2}{4} L_c \tag{A.18}$$

A.4. IEC limit flexural

The Ralston model, based on the plastic behavior of ice failure, is extensively referenced in literature and serves as the sole model presented in the IEC 61400-3 (2009) Standard annex on ice forces. While the IEC version relies on graphical methods, this implementation adopts the analytical formulation from ISO 19906 Annex. The total horizontal force F_H comprises breaking and ride-up components:

$$F_H = H_B + H_R \tag{A.19}$$

with

$$H_B = \sigma_f \frac{h^2}{3} \frac{\tan\alpha}{1-\mu g_r} \left[\frac{1 + Y x \ln x}{x-1} + G(x-1)(x+2) \right] \tag{A.20}$$

where Y is derived from the selected yield criterion (for Tresca criteria: $Y = 2.711$), and G represents a non-dimensional weight-to-strength ratio:

$$G = \left(\frac{\rho_i g w^2}{4\sigma_f h} \right). \tag{A.21}$$

Additionally,

$$x = 1 + \left(3G + \frac{Y}{2} \right)^{-0.5} \tag{A.22}$$

and

$$g_r = \frac{\sin\alpha + \frac{\alpha}{\cos\alpha}}{\frac{\pi}{2}\sin^2\alpha + 2\mu\,\alpha\,\cos\alpha}. \tag{A.23}$$

The ride-up term H_R is given by:

$$H_R = W\left(\frac{\tan\alpha + \mu E_2 - \mu\, f\, g_r \cos\alpha}{1-\mu g_r} \right) \tag{A.24}$$

where W, the weight of ice riding up the cone, is:

$$W = \rho_i\, g\, h_d \left(\frac{w^2 - w_T^2}{4\cos\alpha} \right) \tag{A.25}$$

where h_d is the ride-up thickness (typically 2–3 times ice thickness h for pile-up modeling) and w_T as cone top diameter. Also,

$$f = \sin\alpha + \mu\, E_1\, \cos\alpha. \tag{A.26}$$

E_1 and E_2 are complete elliptic integrals of the first and second kind:

$$E_1 = \int_0^{\pi/2} (1 - \sin^2\alpha\ \sin^2\eta)^{-0.5} d\eta \tag{A.27}$$

$$E_2 = \int_0^{\pi/2} (1 - \sin^2\alpha\ \sin^2\eta)^{0.5} d\eta \tag{A.28}$$

All other variables follow previous definitions.

References

Abdelhady, H.U., Cannon, D., Fujisaki-Manome, A., Gronewold, A., Wang, J., 2025a. The spatiotemporal dynamics of heatwaves and cold-spells in earth's largest freshwater systems. Geophys. Res. Lett. 52 (14) e2025GL116548.

Abdelhady, H.U., Fujisaki-Manome, A., Cannon, D., Gronewold, A., Wang, J., 2025b. Climate change-induced amplification of extreme temperatures in large lakes. Commun. Earth Environ. 6 (1), 375.

Barooni, M., Nezhad, S.K., Ali, N.A., Ashuri, T., Sogut, D.V., 2022. Numerical study of ice-induced loads and dynamic response analysis for floating offshore wind turbines. Marine Struct. 86, 103300.

Cannon, D., Wang, J., Fujisaki-Manome, A., Kessler, J., Ruberg, S., Constant, S., 2024. Investigating multidecadal trends in ice cover and subsurface temperatures in the laurentian great lakes using a coupled hydrodynamic-ice model. J. Clim. 37 (4), 1249–1276.

Chen, C., Beardsley, R., Cowles, G., 2006. An unstructured grid, finite-volume coastal ocean model (fvcom) system. Oceanography 19 (1), 78–89.

Chen, C., Liu, H., Beardsley, R.C., 2003. An unstructured grid, finite-volume, three-dimensional, primitive equations ocean model: application to coastal ocean and estuaries. J. Atmos. Oceanic Technol. 20 (1), 159–186.

Etemaddar, M., Hansen, M. O.L., Moan, T., 2014. Wind turbine aerodynamic response under atmospheric icing conditions. Wind Energy 17 (2), 241–265.

Fang, H., Duan, M., Xu, F., Shen, Z., Liu, Y., 2000. Reliability analysis of ice-induced fatigue and damage in offshore engineering structures. China Ocean Eng. 14 (1), 15–24.

Fujisaki, A., Wang, J., Bai, X., Leshkevich, G., Lofgren, B., 2013. Model-simulated interannual variability of lake erie ice cover, circulation, and thermal structure in response to atmospheric forcing, 2003-2012. J. Geophys. Res. Oceans 118 (9), 4286–4304.

Fujisaki-Manome, A., Cannon, D., King, K., 2024. Daily mean air temperature data for the north american Great Lakes based on coastal weather stations; (ncei accession 0291722.

Gao, G., Chen, C., Qi, J., Beardsley, R.C., 2011. An unstructured-grid, finite-volume sea ice model: Development, validation, and application. J. Geophys. Res. Oceans, 116 (C8). https://doi.org/10.1029/2010JC006688

Guest, P., Luke, R., 2005. Vessel icing. Marine Weather Log 49 (3). https://vos.noaa.gov/MWL/dec_05/ves.shtml

Hammer, T.C., Willems, T., Hendrikse, H., 2023. Dynamic ice loads for offshore wind support structure design. Marine Struct. 87, 103335.

Hawley, N., Beletsky, D., Wang, J., 2018. Ice thickness measurements in lake erie during the winter of 2010-2011. J. Great Lakes Res. 44 (3), 388–397.

Hersbach, H., Bell, B., Berrisford, P., Hirahara, S., Horányi, A., Muñoz-Sabater, J., Nicolas, J., Peubey, C., Radu, R., Schepers, D., et al., 2020. The era5 global reanalysis. Q. J. R. Meteorol. Soc. 146 (730), 1999–2049.

Hibler III, W., 1979. A dynamic thermodynamic sea ice model. J. Phys. Oceanogr. 9 (4), 815–846.

Huang, Y., Zhou, J., Zhu, B., Tian, Y., 2025. Regime-based fatigue damage evaluation and mitigation in offshore wind turbines under wind-ice loading. Ocean Eng. 341, 122480.

Hunke, E., Lipscomb, W., 2006. Cice: the los alamos sea ice model documentation and software user's manual, report, Los Alamos NATL. Lab. Los Alamos, NM.

Hunke, E.C., 2001. Viscous-plastic sea ice dynamics with the evp model: Linearization issues. J. Comput. Phys. 170 (1), 18–38.

Hunke, E.C., Dukowicz, J.K., 1997. An elastic-viscous-plastic model for sea ice dynamics. J. Phys. Oceanogr. 27 (9), 1849–1867.

Hunke, E.C., Dukowicz, J.K., 2002. The elastic-viscous-plastic sea ice dynamics model in general orthogonal curvilinear coordinates on a sphere-incorporation of metric terms. Mon. Weather Rev. 130 (7), 1848–1865.

IEC 61400-3 2009. Wind turbines-part 3: design requirements for offshore wind turbines. In: Proceedings of the IEC, pp. 61400–61403.

ISO 19906, 2010. Petroleum and natural gas industries-arctic offshore structures. Technical Report. ISO. Geneva, Switzerland.

Javaherian, M.J., Cannon, D., Wang, J., Fujisaki-Manome, A., Bai, P., Zuo, L., 2025a. Simulating ice-wave interactions in the laurentian great lakes using a fully coupled hydrodynamic-ice-wave model. Ocean Modelling.

Javaherian, M.J., Wang, A., Hall, L., Zuo, L., 2025b. Offshore wind development in the great lakes: challenges, resources and technical solutions. Ocean Dyn. 75 (3), 1–25.

Lipscomb, W.H., Hunke, E.C., Maslowski, W., Jakacki, J., 2007. Ridging, strength, and stability in high-resolution sea ice models. J. Geophys. Res. Oceans 112 (C3). https://doi.org/10.1029/2005JC003355

Lopez, A., Green, R., Williams, T., Lantz, E., Buster, G., Roberts, B., 2022. Offshore wind energy technical potential for the contiguous united states [slides]. Technical Report. National Renewable Energy Lab.(NREL). Golden, CO, USA.

Määttänen, M., 1998. Numerical model for ice-induced vibration load lock-in and synchronization. In: IAHR Symposium on Ice. 1998, 26.-31.7. 1998, Potsdam, NY, Balkema, pp. 923–930.

Mccoy, T.J., Brown, T., Byrne, A., 2014. Ice load project final technical report. Technical Report. Technical report. Seattle, WA (United States).

Mesinger, F., Dimego, G., Kalnay, E., Mitchell, K., Shafran, P.C., Ebisuzaki, W., Jović, D., Woollen, J., Rogers, E., Berbery, E.H., Ek, M.B., Fan, Y., Grumbine, R., Higgins, W., Li, H., Lin, Y., Manikin, G., Parrish, D., Shi, W., 2006. North american regional reanalysis. Bull. Am. Meteorol. Soc. 87 (3), 343–360.

Minallah, S., Steiner, A.L., 2021. The effects of lake representation on the regional hydroclimate in the ecmwf reanalyses. Mon. Weather Rev. 149 (6), 1747–1766.

Musial, W., Green, R., Demeo, E., Cooperman, A., Housner, S., Marquis, M., Macdonald, S., Mcdowell, B., Hein, C., Rolph, R., et al., 2023. Great lakes wind energy challenges and opportunities assessment. Technical Report. National Renewable Energy Lab.(NREL). Golden, CO, (United States).

Musial, W., Ram, B., 2010. Large-scale offshore wind power in the united states: Assessment of opportunities and barriers. Technical Report. National Renewable Energy Lab.(NREL). Golden, CO (United States).

NREL, 2023. Exploring offshore wind energy opportunities in the great lakes. Accessed: 2025-12-17.

NYSERDA, 2022. New York State Energy Research and Development Authority, New York State Great Lakes Wind Energy Feasibility Study. Technical Report, 22-12, New York State,Albany, NY.

Okulov, V., Kabardin, I., Mukhin, D., Stepanov, K., Okulova, N., 2021. Physical de-icing techniques for wind turbine blades. Energies 14 (20), 6750.

Overland, J.E., 1990. Prediction of vessel icing for near-freezing sea temperatures. Weather Forecasting 5 (1), 62–77.

Overland, J.E., Spindler, T., 2025. A Review of NOAA's Vessel Spray Prediction System.

Shi, W., Liu, Y., Wang, W., Cui, L., Li, X., 2023. Numerical study of an ice-offshore wind turbine structure interaction with the pile-soil interaction under stochastic wind loads. Ocean Eng. 273, 113984.

Simmons, A., Hersbach, H., Munoz-Sabater, J., Nicolas, J., Vamborg, F., Berrisford, P., Rosnay, P.D., Willett, K., Woollen, J., 2021. Low frequency variability and trends in surface air temperature and humidity from ERA5 and other datasets. European Centre for Medium-Range Weather Forecasts.

Sutherland, C.L., Scanlan, M.K., 2025. Great lakes offshore wind: An analysis of coastal management planning tools. Notre Dame J. Emerging Tech. 6, 308.

Tammelin, B., Cavaliere, M., Holtinnen, H., Morgan, C., Seifert, H., Säntti, K., 2000. Wind energy in cold climate. Technical Report Report WECO Finnish Meteorological Institute Helsinki, Finland.

Thorndike, A.S., Rothrock, D.A., Maykut, G.A., Colony, R., 1975. The thickness distribution of sea ice. J. Geophys. Res. 80 (33), 4501–4513.

Tikanmäki, M., Heinonen, J., Jokiniemi, A., Eriksson, P.B., 2025. Design sea ice conditions for offshore wind power in the baltic sea. Cold Reg. Sci. Technol. 234, 104463.

Titze, D., Austin, J., 2016. Novel, direct observations of ice on lake superior during the high ice coverage of winter 2013-2014. J. Great Lakes Res. 42 (5), 997–1006.

Wang, J., Bai, X., Hu, H., Clites, A., Colton, M., Lofgren, B., 2012. Temporal and spatial variability of great lakes ice cover, 1973-2010. J. Clim. 25 (4), 1318–1329.

Wang, J., Xue, P., Peco, K., Huang, C., Pringle, W.J., Yang, Z., Chakraborty, T., Qian, Y., Hetland, R.D., 2025. Influence of lake ice biases in reanalysis data on downscaled climate simulations over the great lakes region. Authorea Preprints.

Weeks, W.F., Ackley, S.F., 1986. The growth, structure, and properties of sea ice. Springer.

Wu, T., Yang, H., Wang, P., Zhang, C., Zhang, M., 2024a. Data-driven fatigue reliability evaluation of offshore wind turbines under floating ice loading. J. Struct. Eng. 150 (12), 5024004.

Wu, T., Zhang, M., Peng, R., Yu, H., 2024b. Numerical study on ice-induced vibration control of a 10-mw monopile offshore wind turbine using tuned mass damper. Ocean Eng. 311, 118909.

Xue, P., Ye, X., Pal, J.S., Chu, P.Y., Kayastha, M.B., Huang, C., 2022. Climate projections over the great lakes region: using two-way coupling of a regional climate model with a 3-d lake model. Geosci. Model Dev. 15 (11), 4425.

Zhang, Z., Zhang, H., Zhang, X., Hu, Q., Jiang, X., 2024. A review of wind turbine icing and anti/de-icing technologies. Energies 17 (12), 2805.

Zhu, B., Sun, C., Jahangiri, V., 2021. Characterizing and mitigating ice-induced vibration of monopile offshore wind turbines. Ocean Eng. 219, 108406.

Zou, P., Bricker, J.D., Fujisaki-Manome, A., Garcia, F.E., 2024. Characteristics of ice-structure-soil interaction of an offshore wind turbine. Ocean Eng. 295, 116975.